The Dissertation Committee for Max Sasha Daniller-Varghese
certifies that this is the approved version of the following dissertation:

Unsteady and Heterogeneous Boundary Conditions and their Impact on Sediment Transport and Landscape Morphology

Committee:

David C Mohrig, Co-Supervisor

Wonsuck Kim, Co-Supervisor

Paola Passalacqua

Daniella Rempe

Paul Myrow

Unsteady and Heterogeneous Boundary Conditions and their Impact on Sediment Transport and Landscape Morphology

by

Max Sasha Daniller-Varghese

DISSERTATION

Presented to the Faculty of the Graduate School of

The University of Texas at Austin

in Partial Fulfillment

of the Requirements

for the Degree of

DOCTOR OF PHILOSOPHY

THE UNIVERSITY OF TEXAS AT AUSTIN

August 2019

To you.

Acknowledgments

There are so many people to thank, I hardly know where to start. I would like to thank my advisors, my colleagues and friends, and my family, whose love and support buoyed me through all the hard parts. And lastly, to my love, Caitlin. I could not have done it without you.

Unsteady and Heterogeneous Boundary Conditions and their Impact on Sediment Transport and Landscape Morphology

Max Sasha Daniller-Varghese, Ph.D.
The University of Texas at Austin, 2019

Co-Supervisors: David C Mohrig
Wonsuck Kim

While sediment transport and landscape morphology are well-characterized under the simplifying conditions of steady and uniform inputs, the effects of heterogeneity and unsteadiness are less well-constrained. This dissertation investigates the effects of heterogeneous and fluctuating inputs on upland sediment transport, coastal margin morphology and sediment routing, and turbidity current dynamics and deposition. In my first project, I characterize how cycles of flooding and normal flow influence delta island shape and evolution. Using the Surface Transport and Earth-surface Processes (STEP) Basin, located at the Morphodynamics Lab at the J. J. Pickle Research Center, I determine the morphological effects of mixed transport type, where sediment is alternately suspended and delivered as bedload in floods and normal flow. The cumulative effect of these types of transport forms a flow bifurcation around a delta island. I find that delta islands are a consequence of mixed transports, rather than an invariant consequence of turbulent jet expansion into a still basin. Second, I investigate the effects that surface waves have in affecting turbidity current sediment transport and mixing. I conducted experiments in the

Long Flume at the Experimental Sedimentology Lab, running simulated turbidity currents through a wave field. After applying a mixing model, I determine that a wave field fundamentally changes the mixing and turbulent behavior of a turbidity current, leading to an increase in downslope sediment transport. Lastly, I investigate dense tracer particle transport in an experimental fluvial bedform, also in the Long Flume. I find that dense tracer minerals' transport is decoupled from bulk quartz sediment bedload transport. Collectively, these investigations represent a synoptic view of sediment transport and the effect that unsteadiness and heterogeneity have on dynamics of sediment transport and consequent morphology of sedimentary landscapes.

Table of Contents

List of Tables

List of Figures

Chapter 1

Introduction

Natural systems are seldom steady or uniform, on short or long timescales. This dissertation is, broadly speaking, focused on morphodynamics. I aim to examine how unsteady and heterogeneous signals from flow, and change sediment transport, and affect landscape evolution. The three projects which make up this dissertation encompass transport and depositional systems involved in preserving these signals in the topography and the sedimentary record.

Chapter 2 examines river-dominated deltas. The dimensions and organization of deltaic islands and channels dictate delta morphology. I present experimental results modeling deposition at a river mouth and flow bifurcation around delta islands. Mouth bar formation and channel bifurcation is achieved in a laboratory setting by alternating input of suspended load transport and bedload transport. These two modes of transport produce two characteristic deposits with different advection lengths. Suspended load transport creates a steep deposit far from the inlet, while bedload creates a low angle, leveed deposit near the inlet. I found that flow bifurcations occur where the proximal and distal deposits encroach on one another. I determine that there is a relationship between the frequency of suspended load transport and the length to channel bifurcation. Frequent flooding causes shorter length to bifurcations, whereas infrequent flooding causes greater length to bifurcations. This work overturns the hitherto understood mechanism of bifurcation location as a function of only high-transport conditions. Instead, the interactions between the sediment transport and deposition from normal flow and large-scale flooding events dictate delta island morphology.

Chapter 3 focuses on near-shore shallow marine to deep-ocean signal propagation in a turbidity current. In shallow-marine environments gravity-driven currents like sediment-laden hyperpycnal flows often traverse shallow waters under the influence of surface wave fields. The resulting flows are key drivers of offshore sediment transport. Our laboratory experiments illustrate how surface waves alter sediment transport in gravity-driven density currents. The addition of a wave field to a gravity-driven current resulted in an increase in the downslope transport of the deposit volume. Additionally, oscillatory velocities recorded at downslope locations in surface-wave-altered turbidity-currents were larger than wave field velocities measured at the same location. These observations indicate that surface waves alter turbidity-currents in a longitudinally complex manner whereby the influence of oscillatory currents is transported downslope within the body of the turbidity-current. I also measure the turbulence within the body of the current, and find that combined flows have differing turbulent structures within. I apply an eddy viscosity model to the data and find that the mixing dynamics of combined flows are different than turbidity currents without waves.

These effects were observed in the case of minimal wave input: the maximum orbital velocities of the wave field were an order of magnitude less than the maximum unidirectional velocities of the current. I predict that if the velocities of the wave field and the current were sub-equal, a plausible scenario for hyperpycnal flows in near-shore, deltaic, and proximal shelf environments, these mechanisms would be substantially more effective. This work has significant implications for modeling offshore sediment transport in shallow marine environments and for interpreting the deposits of such flows, most notably that the presence or absence of symmetrical ripples might not indicate whether the current was deposited above or beneath wave-base.

Chapter 4 examines a much smaller-scale set of sediment transport, dense tracer grain transport in a single bedform. Dense tracer particles like detrital zircons are a commonly used to fingerprint provenance. The difference in transport rates and times of different density particles, such as detrital zircons in quartz sand, is critically important to accurately assessing sediment provenance. Because zircons are typically twice as dense as surrounding sediment, and because transport rate scales inversely with grain density, I predicted zircon transport rate as bedload will be smaller than that of quartz sand. Bedforms can also separate the population of zircons along their length, trapping grains in their topographic lows, filtering the grains as they transport them. Moreover, intermittent transport conditions, sediment segregation into floodplains, or preferential sequestration in deep pools can add substantial time lag. I generated a single bedform and allowed it to translate a single wave length. I measured magnetic particle concentration and grain size within the bedform and found that the concentration profile of dense tracers is diagnostic of the vigor of transport of bulk sediment and the dense tracer. After applying an inverse model to determine the grain-scale conditions, and comparing it to our measured dense grain concentrations and grain sizes, I characterize the different ways dense grains transport in bulk sediment and provide some suggestions for representative sampling.

Chapter 2

The Effect of Flood Intermittency on Bifurcations in Fluviodeltaic Systems: Experiment and Theory

Author's note: as of this writing, the materials in this chapter have been submitted to Sedimentology*, and have been accepted, pending minor revision.*

2.1 Introduction

2.1.1 Objectives

Sediment is the sustaining resource to any coastal system. In river-dominated environments, sediment aggrades into landforms near the inlet. In systems like the Mississippi River Delta, the region is artificially leveed to the point where the river is now a strong conduit for sediment. Rather than nourishing the wetlands along the river, sediment bypasses to the farthest point of the delta, far from where it is needed. As the delta deposit dewaters and compacts from natural subsidence and fluid removal, the entire coastal region is threatened by rising sea level (Blum and Roberts, 2009, 2012). One proposed solution is to make controlled river diversions along the river to nourish critical areas with sediment (Kim et al., 2009). If our aim is not only mitigating land loss on the short term, but also creating self-sustaining environmental policies, one must understand the complexities of land growth and evolution (Norton, 2005; CPRA, 2017, 2019). In this chapter I document the full river bifurcation process, achieved for the first time in a laboratory setting under intermittent discharge conditions, and present a more in-depth experimental investigation on the process of island development in fluviodeltaic settings. By varying the flood frequency between experiments, I determine the effects of flooding on the length to bifurcations. I also discuss how natural flood frequency is related to bifurcation length.

2.1.2 Background

Deltas are fundamentally constituted of islands and the branching channels around them (Hiatt and Passalacqua, 2015; Passalacqua, 2017). Therefore, considering the scaled length to bifurcation around an island is an appropriate metric for characterizing a river delta morphology (Edmonds and Slingerland, 2007). Delta islands form when a sediment-laden flow enters slack water; the flow loses momentum and carrying capacity and then deposits its sediment. As sediment accumulates a bar in front of a channel, flow bifurcates around the sediment deposit and sediment continues to aggrade. Once the deposit breaks the water surface or is colonized by vegetation, it may be called an island. Deltas are made of successive channel bifurcations and aggrading islands. The work by Hiatt and Passalacqua argued that channels and islands were far more interconnected than previously thought, and could not be easily separated into rigid categories of island nodes and channel connections. Similarly, I view channel-island units as the fundamental part of delta systems. With that in mind, understanding how a single unit evolves over time and under different external forcings should be an important first step to understanding how larger delta systems behave. The Intermittency factor, I, characterizes periods of threshold morphodynamic activity and inactivity, and is a prevalent simplification throughout field data analysis, experimental simulations, and numerical models (Paola et al., 1992; Parker et al., 1998). This assumption allows models to set sediment transport as steady and uniform and simply adjust the intermittency. However, work by Shaw and Mohrig (2014) shows that even during low-flow conditions there is substantial reworking of sediment and bedload sediment transport in deltaic systems. The effects of varying intermittency have been studied experimentally, but synoptically, examining the effect of intermittency over an entire delta's morphology (Piliouras et al., 2017). Our work determines the effect of intermittency on the smaller scale constituent units (i.e., channel bifurcations and delta islands) that make up a delta. Our aim is to understand how early-stage delta islands evolve over time depending on intermittent flow discharge and its frequency. Early work conceptualized deposits at river mouths, referred to generically as "mouth bars," or, "bars," as the result of expanding jet flow from a confined river to an unconfined basin (Bates, 1953; Wright, 1977). When a river empties into a basin, the flow decelerates like a turbulent plane jet. The jet's center decelerates as a function of the square root of the distance and has a strong lateral dispersive component (Bates, 1953). Levees deposit near the river mouth because this lateral flow drops below the critical shear stress to transport sediment. As the jet moves farther into the basin and expands, its overall velocity decreases. At the location where flow velocity is below the critical threshold for sediment mobility, the jet deposits its sediment load. Flow then bifurcates around this deposit. The drag of the deposit on subsequent flow creates preferential deposition on the bar top. There are several types of mouth bar development as a result of different jet friction parameters and hyperpycnal and hypopycnal jets, but in every case the larger scale structure of a river delta is the result of mouth bars developing into islands in succession with one another, and in this way they are the "fundamental element" of a delta system (Wright, 1977).

Numerical models have been a productive method of inquiry for understanding delta and mouth bar formation. Delft3D has been used to a great extent to model system-wide evolution and its response to an allogenic forcing and autogenic dynamics (Lesser et al., 2004). Mouth bar formation has been addressed with a morphodynamic model that solves the depth averaged Navier-Stokes equations with a $k - \epsilon$ closure model (Edmonds and Slingerland, 2007). Edmonds and Slingerland found that the incidence of mouth bar formation, and the location of channel bifurcation occurred at the incidence of minimum divergence in sediment transport as the input turbulent jet expands into the basin. These models rely on specific assumptions that reduce complexity in the fluid and sediment behavior, as well as the scale and frame of reference. This is out of necessity, making the equations tractable, solvable, and able to approximate the systems to a high degree of precision. In these models, bifurcation is a function of hydrodynamic input conditions. Experimentally, Rowland et al. (2009) examined sedimentation at a channel mouth by a turbulent jet, which was in general a similar condition with the numerical models. Rowland et al. (2009), considered turbulence, lateral meander, and the buoyancy of the jet. While they could generate levees by lateral dispersive flux, they could neither create mouth bars nor any flow bifurcation. One important conclusion they drew was that suspended sediment load played a larger role than previously thought on levee formation. Shaw and Mohrig (2014) showed the importance of interflood flow on the dynamics of the Wax Lake Delta, Louisiana, USA, where the distal extension of the delta network was strongly influenced by interflood conditions, rather than just threshold discharge. The subaqueous channels substantially eroded and extended during seasonal-scale low flow conditions. Their work shows that the formative discharge simplification needs reassessment, recasting work by Parker et al. (1998) and Paola et al. (1992) and used throughout field data analysis, experimental simulations, and numerical models, and that allowed for conceptualizing systems with steady and uniform flow. Our work aims to experimentally investigate interflood flow's effect on landscape evolution, testing the degree to which flood and interflood interactions dictate the length to delta islands.

2.2 Methods

Twelve experiments were conducted in the Sediment Transport and Earth-surface Processes (STEP) Basin, located in the Morphodynamics Laboratory at the University of Texas at Austin. In each experiment, the domain is $1.85\,m \times 2\,m$ with water depth of $50\,mm$ over a $50\,mm$ thick sediment bed (Figure 2.1). The sediment bed acts as a rough base and ensures the flows are transport-limited rather than supply-limited. At every moment the flow transports as much sediment as it is capable of. The bed is composed of the same grain size as the input sediment. A computer controlled pump and auger feed the sediment and water ($0.355\,l/s$ at a concentration of $1:100$) mixture into a bucket with an Arduino-controlled knife valve that connects to the domain inlet by a 2 inch PVC pipe. The supplied sediment is composed of fine quartz sand, with a D_{50} of 171 $\mu\,m$ and a density of 2650 kg/m^3. The water level in the STEP basin is maintained by a computer controlled weir, constraining water level within 1 mm of the 50 mm above the initial sediment bed height. The tank does not recirculate, and all the sediment from the flows remains in the domain during the experiments.

During floods, the knife valve closes for a programmed duration of 15 s, blocking flow into the flume and filling the bucket to 5.325 l, and then opens for a 0.89 s duration flood and subsequent interflood flow. The inlet hose is placed at an angle to the bucket wall, forming a strong circulation cell in the bucket that keeps sediment in suspension. Because the system is pre-programmed through the Arduino, the floods are all the same discharge of 6 l/s, while interflood discharge is 0.355 l/s. This setup also allows for broad comparability across different runs with different intermittencies. Each run receives the same sediment and water volume input, and the magnitude of each individual flood is the same. The only changing variable from experiment to experiment is the frequency of flooding (Table 2.1).

The aim of bimodal flow conditions in a single experiment is to simulate two types of sediment transport (Table 2.2). The Rouse number ($P = w_s/\kappa u_*$), calculated by determining the ratio of a grain's settling velocity (w_s) and the shear velocity (u_*)multiplied by von Karman's constant ($\kappa = 0.41$), is a useful metric for determining transport mode. When $P < 1$, the transport mode is full suspension, and when $P > 2.5$, the transport is primarily bedload (Bagnold, 1966; Nishimura and Hunt, 2000; Niño et al., 2003). Rouse Number calculations and observations show that our flow during interflood conditions transports grains as bedload with possible incipient suspension ($P = 2.96$), while the floods in the experiments move grains in full suspension ($P = 0.18$). These two Rouse Number conditions generate two inlet advection lengths. One is associated with levee construction and sedimentation within channels and the other with grains settling out of the fluid column. I conducted experiments at a range of flood intermittencies, with floods ranging from once every 1 min to every 20 min; a 10 min experiment adding additional sediment during floods. I also ran experiments with low flow with no floods, and successive floods only (Table 2.1).

The experiments were recorded with overhead time-lapse imagery, a photo taken every 15 seconds. The overhead images were preprocessed, correcting for lens distortions at the edge of the frames. The images were further processed to visualize channel residence by binarizing the image so dyed water and sediment are separated into black and white pixels, after Tal and Paola (2007). The topset area was determined by counting the number of white pixels in the processed image. Topography scans were taken at hourly intervals with a Keyence laser altimetry scanner attached to an automated cart system that scanned the entire deposit with a horizontal grid resolution set to 1 mm down dip by 10 mm in strike with vertical sub-millimeter resolution. I have uploaded our data to the SEAD data repository and the Texas Data Repository (https://sead2.ncsa.illinois.edu/, http://doi.org/10.5967/M0BZ645X, and http://data.tdl.org/, DOI in prep).

2.3 Experimental Results

2.3.1 Experimental Bifurcation Processes

In the following subsections, I consider a single experimental single time series (Figure 2.2) with floods every 10 minutes, documenting the full evolution of mouth bar formation and channel bifurcation. Following that, I report results from all other experiments in the ensemble, investigating the control of intermittency on the length to bifurcation.

2.3.1.1 Sediment Transport: Levees in the Proximal, Lunate Bars in the Distal

As discussed above, the two experimental flow regimes result in two distinct types of sediment transport, and two consequent deposits. I can see this in Figure 2.2A and Figure 2.2B, with distinct sediment deposits proximally and distally. Interflood transports sediment as bedload (Rouse number, $P = 2.96$) and results in a leveed channel near the inlet. Floods result in full suspension of the material at the inlet ($P = 0.18$) and develop deposits $0.8\,m$ downstream of the inlet, which are reminiscent of lunate bars (Figure 2.2B), first described by Bates. The distance to bar deposits is determined by the advection velocity, the grain settling velocity, and the depth of the water. Flooding re-entrains sediment in the trunk channel, developing stronger channelization and transporting the sediment to the distal bar deposit. The trunk channel profile maintains a convex up shape in this early stage (Figure 2.3B). With time, distal flood deposits prograde basinward and aggrade above the water surface (Figure 2.2B, Figure 2.2B, and 2.3A). They become the highest point in the domain, though they sometimes are equal elevation to the levees in the proximal

(Figure 2.3A).

2.3.1.2 Channel Bifurcation

Bifurcation occurs as proximal deposits encroach on the distal flood deposit. In Figure 2.2C, I observe the intersection of the two deposits, and subsequent channel bifurcation in Figure 2.2D. The leveed proximal deposit directs interflood flow to the steep, distal deposit (Figure 2.2C, 2.3A and 2.3B). The flow does not uniformly cover the bar surface, and forms two deeper flows around it. Figure 2.4 shows time accumulative maps of focused flow (water depth deeper than 5 mm), each over one fifth of the duration in an interflood period. In the earlier stage of bifurcation at runtime = 131 though 139 min (Figure 2.4A), floods develop a parabolic distal bar (Figure 2.4A1) with two sides extended upstream. This bar migrates basinward in the early stage before the bifurcation occurs. The flood is uneven laterally across the bar but still flows over the center of the bar where the elevation is the highest. Interfloods gradually erode the sides of the bar and deposit sediment at the center of the flow divergence and change the bifurcation angle (Figure 2.4A2-3). Deposition also starts at the tips of the bifurcated two channels and backfills the main trunk channel (Figure 2.4A4-5). In the early stage in bifurcation the bifurcated channels are underfilled throughout the interflood periods compared to the later stages in bifurcation (Figure 2.4A). In the later stage of bifurcation at runtime = 251 through 259 min, the bifurcation angle closes from 126 degrees to 99 degrees (Figure 2.4B). Flood flow is split into two channels and makes deposit at each end of the channels (Figure 2.4B1). During the interflood, the channels are significantly filled and only the upstream end near the inlet is maintained (Figure 2.4B2-3). Toward the end of interflood periods in the later stage, the surface topography becomes smoother, and the distal bar deposit and proximal leveed deposit encroach upon each other (Figure 2.4B4-5).

2.3.1.3 Autochannelization and Topographic Reworking

One limitation of our experimental setup is a lack of cohesion in our deposit. Without cohesion, sediment is readily eroded, and second order bifurcations are unable to develop. This is because the daughter channels migrate too quickly to generate stable bars at their mouths, or the trunk channel oversteepens and reworks the distal island. The elevation difference between the main channel and the bar decreases as the trunk channel fills with sediment and the distal island slows aggradation (Figures 2.3E and 2.3F). Channels stop bifurcating and begin migrating when the levee height reaches the same height as the distal island, and the channel incises into the distal deposit (Figure 2.2E and Figure 2.2F). While intermittent floods rework and redeposit sediment to a certain degree, the channels have some memory and often follow their former paths. Either one channel is preferentially occupied and sweeps across the island (Figure 2.2E), or the proximal deposit steepens to the degree that the distal deposit is at equal elevation, and the occupied channel erodes through it (Figure 2.2F). Following either of the scenarios, or both in sequence, the local shoreline at the channel tip progrades through and beyond the island. The consequence of autochannelization in these experiments is a long, straight channel from the inlet to beyond the distal island (Figure 2.2F, 2.3B at 360min).

2.3.1.4 Bifurcation Length as a Function of Intermittency

In this subsection, I report the results of our other experiments, focusing on the bifurcation length as a function of flooding frequency (Figure 2.2D). A series of experiments were conducted with a continuous interflood condition, different flood intermittencies of 20 min, 10 min, 7.5 min, 5 min, and 4.05 min, and a continuous flood condition (Table 2.1). In Figure 2.5 I present a subsample of time-lapse overhead images for a range of the experiments I conducted. The first-order morphological difference between runs is distribution of mass. Continuous flood and higher flood frequency runs (Figure 2.5, row 1, row 2 and row 3) have more sediment deposited distally from the inlet. Infrequent flood runs develop longer and wider levee deposits in the proximal region. A broad range of bifurcation lengths is possible from flooding frequency change (Figure 2.6). The bifurcation length, the most notable and simply characterized parameter (Figure 2.2), has a strong dependence on the frequency of flooding. I measure a distance from the inlet to the unwetted distal bar surface during interflood flow, our definition of island position and incidence of bifurcation as a bifurcation length. Experiments with infrequent flooding (i.e., 20 min between floods), have a greater bifurcation length, while those that frequently flood (4.05 min between floods) have a shorter bifurcation length (Figure 2.5, row 5, column 5 and row 2, column 5).

2.4 Discussion

2.4.1 Bifurcation Mechanism

Instead of considering bifurcations as a consequence of steady hydrodynamics and turbulent jet decay, I show how that variability in sediment transport and deposition force the location of a bifurcation. Edmonds and Slingerland (2007) demonstrated that a bifurcation occurs at the minimum divergence of sediment flux transported by a turbulent jet, but the broader applicability of our data to unsteady systems indicates another mechanistic explanation for the location of a first-order bifurcation. Our results show interactions between different types of transport and deposition controlling where bifurcations occur. If bifurcations were purely the result of jet flow into a basin, then the bifurcations in our experiments should be all be the same length from the inlet, because all of our floods are the same magnitude from run to run.

In all of our experiments, bifurcations occur where flood and interflood deposits intersect. The proximal deposits build a sufficiently leveed channel to reach the distal bar; the distal deposit back-fills into the proximal as it radially aggrades with each flood. As flow is routed from the proximal deposit to the distal, the flow becomes unstable and unable to cover the distal deposit uniformly. Consequently, the flow channelizes around the distal region deposit into a bifurcation. Second order bifurcations did not develop primarily because of a lack of cohesion in the bar and channel levee deposits. The daughter channels actively migrated, dispersing sediment, rather than depositing fixed islands. Another possible reason was our constant input of sediment. With smaller input sediment during interflood periods, our flood discharge might have been able to clear the proximal region more effectively and maintain stronger focused flow within confined channels to transport more sediment to new distal mouth bars.

2.4.2 Intermittency and the Consequences for Bifurcation Length

Rather than the traditional hydraulic conception of intermittency, I base our intermittency in terms of inlet sediment transport mode. Intermittency is defined as the ratio of transport duration at the inlet that can move our sediment as suspended load relative to total transport time:

$$I = \frac{t_{floods}}{(t_{floods} + t_{interfloods})}. \tag{2.1}$$

To compare experimental data to natural systems, I introduce a non-dimensional shear stress term, T, that includes I. Shear stress of the flow (τ) is defined as,

$$\tau = \rho_f u_*^2, \tag{2.2}$$

where ρ_f, is fluid density and u_*^2 is shear velocity. T is defined as,

$$T = \frac{\rho_f (I u_{flood}^2 + (1 - I) u_{interflood}^2)}{(\rho_s - \rho_f) g D} \tag{2.3}$$

Where ρ_s is the sediment density, g is acceleration due to gravity, and D is grain size. I acts as a corrective factor to determine the relative contribution of shear stress exerted by floods and interfloods. In these experiments, u_{flood} is the mean velocity when $P > 2.5$, and $u_{interflood}$ is the mean velocity when $P < 2.5$. In a setting with times of no transport, there is a critical Rouse Number, P_c, with u_{*c} defined by Brownlie (1981), and the settling velocity determined by Ferguson and Church

(2004). The relationship factors in the wide range of input fluxes into a system while preserving the effect different modes of transport have on the cumulative force exerted by the flow.

A notable result of these experiments is how bifurcation length is negatively related to flooding contribution (Figure 2.6). The bifurcation location is governed more by deposition during interflow period and flood bar deposit backfill than by jet flow setting a bifurcation point. A crucial insight into how topography determines where bifurcations occur is that suspended load sediment transport has a fixed advection range. In suspended load transport, the travel distance of a particle is set by its settling velocity, the velocity of the flow, and depth of the fluid column. In our experiments, those values are fixed. Over time, the flood-built island initially progrades but then backfills towards the channel mouth and into the proximal deposit. Backfilling occurs because of adverse topography created by prior flooding. The inlet-side of the island aggrades because the floods are unable to transport sediment over the island and to the far side of the island. One can see this most clearly in Figure 2.5, row 2, though it can also be observed in rows 3 through 5 as well. Frequent floods aggrade the island over the duration of the experiment and backfill towards the inlet, rather than migrating distally. The reason that experiments with more frequent flooding have shorter bifurcation lengths is that there is more backfilling into the channel mouth, and less progradation of the leveed channel. Conversely, experiments that flood infrequently have only a small distal deposit, and normal flow can prograde to meet it. Our experiments are highly idealized, but preliminary work indicates applicability to natural systems. The lack of long term and persistently measured velocity data at the apices of natural systems, along with sediment grain size data on islands, within channels, and suspended during flood. Our preliminary model results are encouraging, despite using sparse field data.

Because our model inputs are sensitive to discharge and grain size, the two most uncertain inputs, I can only offer limited applicability to natural deltas (Figure 2.6). The Wax Lake Delta T is plotted on Figure 2.6 by fitting discharge to gauge and limited velocity data from the USGS station at Calumet (USGS 07381590). Grain size of sediment in the channels is taken from Shaw and Mohrig (2014). A script to calculate T, is provided in supplementary materials. The general agreement between our experimental data and the field delta indicate how transport intermittency forces morphology at the island scale. I believe this is an opportunity to taking and reporting new, detailed data at delta apices and grain size data at bifurcations, on islands, and in mouth bars.

2.5 Conclusions

Bifurcation around islands characterizes delta distributary networks. Here I present an ensemble of experiments which show the length to a bifurcation is controlled by the intersection of suspended and bedload deposits. The stages of channel bifurcation around an island are as follows. As a bedload-laden flow empties into a basin, it first forms parallel levees that extend basinward (Figure 2.2A). Cycles of flooding transport sediment in suspension, rework the proximal deposit, and deposit sediment further basinward in a lunate bar (Figure 2.2B). As the proximal deposit aggrades and floods rework it, the distal bar aggrades and expands, backfilling towards the proximal deposit (Figure 2.2C). Once the proximal deposit develops sufficient topography that the floods can no longer entirely rework them with each flood, the proximal deposits prograde toward the distal deposits. The two deposits reach equal elevation and intersect (Figure 2.2C). Flow routes around the steeper distal deposit, bifurcating the channel (Figure 2.2D). After the topset steepens sufficiently, typically one or both of the bifurcated channels erode its outer banks and migrate toward the distal island (Figure 2.2E and Figure 2.2F). This is likely because of lack of cohesion in the experimental deposit.

I find that suspended load transport is limited to a fixed range, so the bifurcation length is set by the degree to which flood deposits backfill towards the channel mouth. Frequent flooding leads to bifurcations more proximally because the bar deposit backfills towards the channel mouth. Infrequent flooding allows interflood flow to transport sediment further basinward and encroach further into the distal deposit. Future work should investigate how to broadly apply this understanding to an ensemble of natural deltas with improved data on estimates of flow velocities at delta apices and grain sizes, as well as how cohesion would improve island bank stability and influence on bifurcation evolution.

Table 2.1: Experiments conducted in the STEP Basin with flood durations ranging from only interflood to successive floods. For all experiments $Q_{sed}/Q_{water} = 1:100$, input discharge, $Q_{water} = 0.355\,l/s$, $u_{flood} = 2.83\,m/s$, $u_{interflood} = 0.17\,m/s$, $P_{flood} = 0.29$, and $P_{interflood} = 4.92$.

Run Number	Interflood Duration (min)	$I = \frac{t_{flood}}{t_{flood}+t_{interflood}}$	$T = \frac{\rho(Iu^2_{flood}+(1-I)u^2_{interflood})}{(\sigma-\rho)gD}$
044	4.05	0.0036	2.0703
023, 031	5	0.0030	1.8705,
040	7.5	0.002	1.5860
024, 034, 036, 039	10	0.0015	1.4436
029	20	0.0007	1.2297
025, 035	only interflood	0	1.0155
026	successive floods	–	290.0731

Table 2.2: Flow parameters of flooding and interflooding conditions.

	$u\ (m/s)$	$u^*\ (m/s)$	$P = w_s/\kappa u^*$	Fr=$\frac{u}{\sqrt{gL}}$	Re=$\frac{uL}{\nu}$
Interfloods	0.17	0.01	3.29	0.24	14.0×10^4
Floods	2.83	0.20	0.19	4.04	0.85×10^4

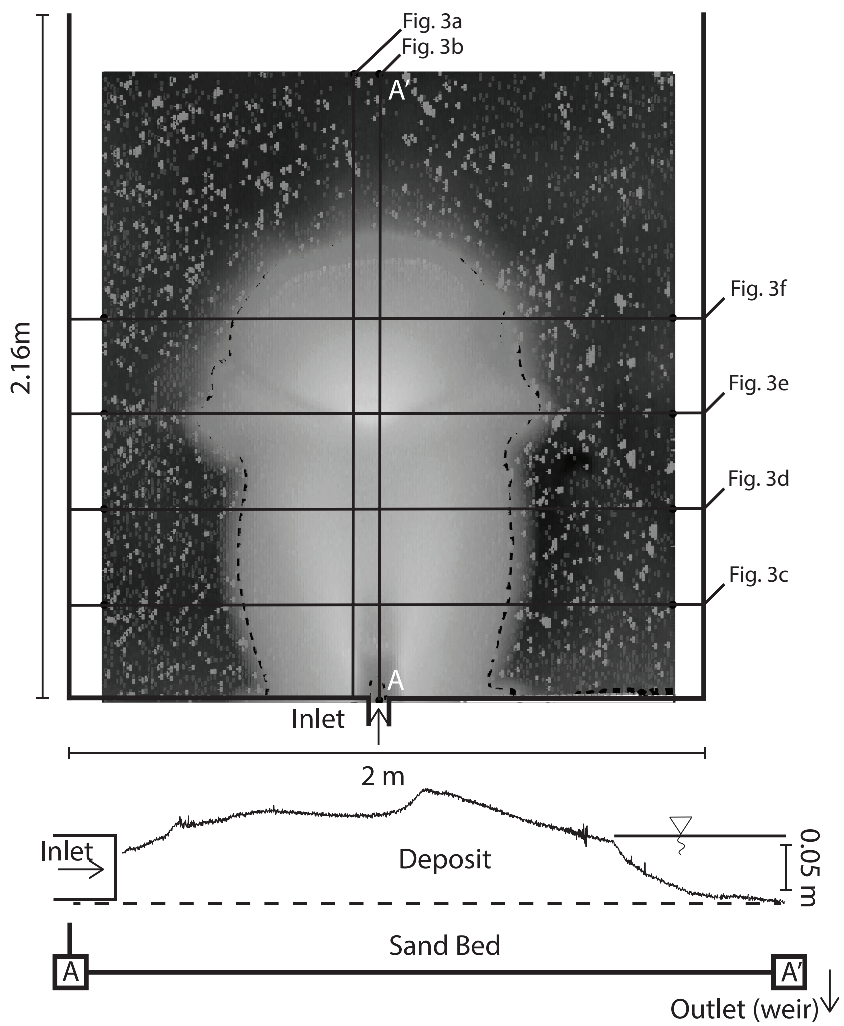

Figure 2.1: STEP Basin with an intermediate deposit (runtime = 240 min). The topographic data was taken from the run with a flood every 10 min.

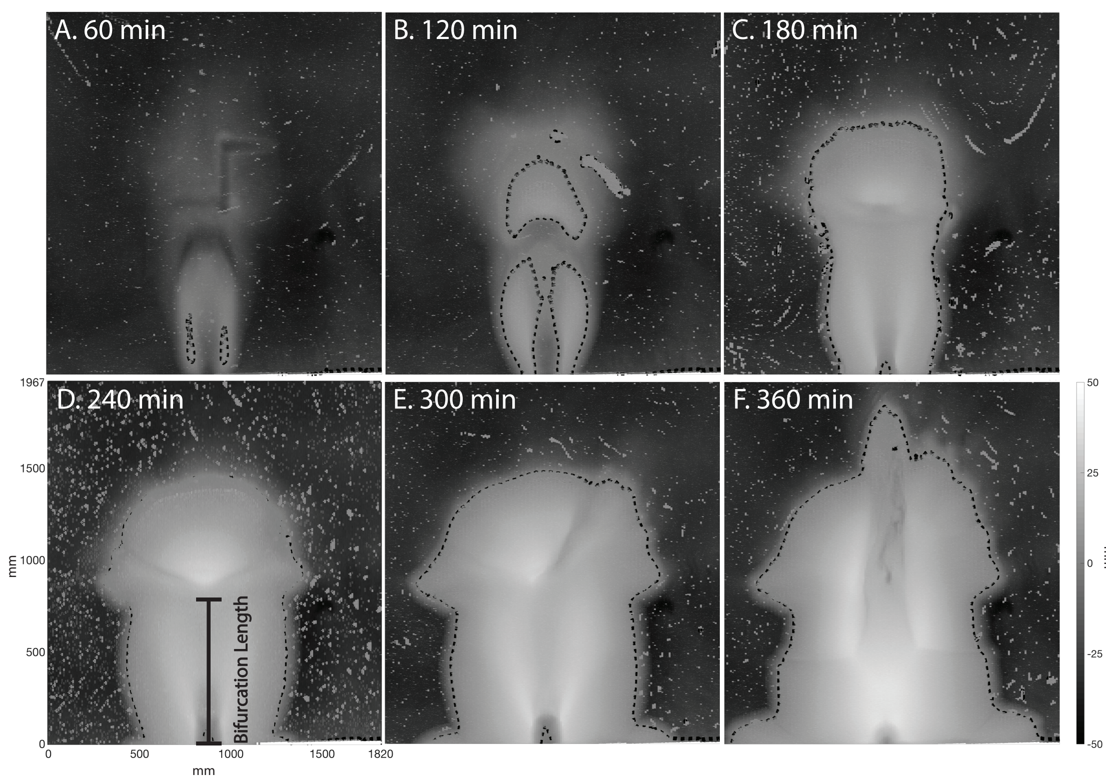

Figure 2.2: Elevation scan time series of an experiment with a flood every 10 min. The dashed line is the ocean level. Initially, levees build out separately from the distal flood deposit, but at runtime = 160 min the two deposits meet and the flow bifurcates. Evidence for this are the lobes of sediment that develop adjacent to the distal deposit–indicating bedload flux during interflood flow around the distal deposit. At runtime = 240 min the deposit is fully bifurcated with incised channels. At runtime = 300 min the topset slope was sufficient for the channel to incise through the distal deposit, and the channel elongated through the flood deposit for the remainder of the experiment (runtime = 360 min).

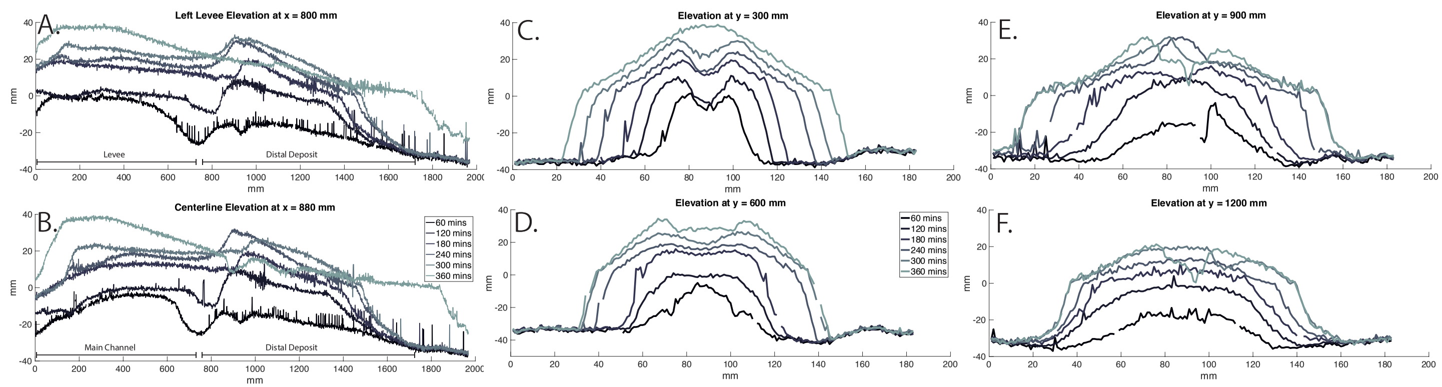

Figure 2.3: Scanned cross sections of the deposit as it evolves over the course of the experiment. Subfigures (A) and (B) are dip profiles, and (C-F) are strike profiles of the proximal deposit's evolution basinward. See Figure 2.1 for the profile locations mapped onto an overhead scan.

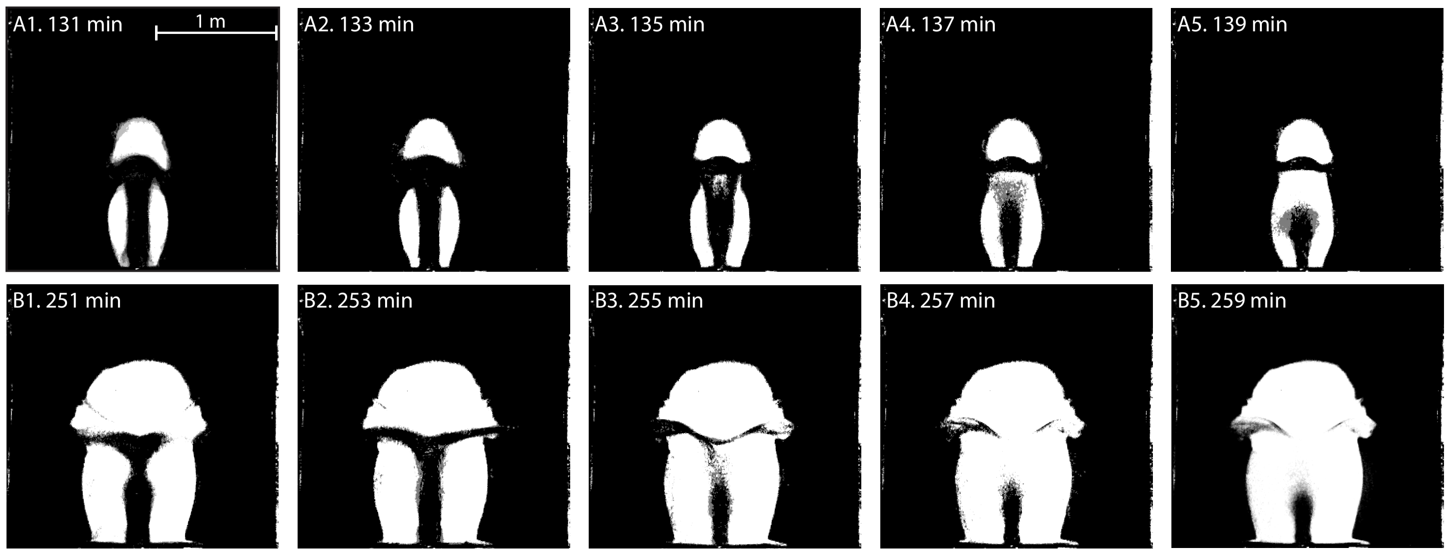

Figure 2.4: Flow maps of the deposit over the course of two interflood cycles (black indicates flow deeper than 5 mm). (A) At the time of channel bifurcation (runtime = 131min), and (B) during a full maturity of the bifurcation (runtime = 251 min).

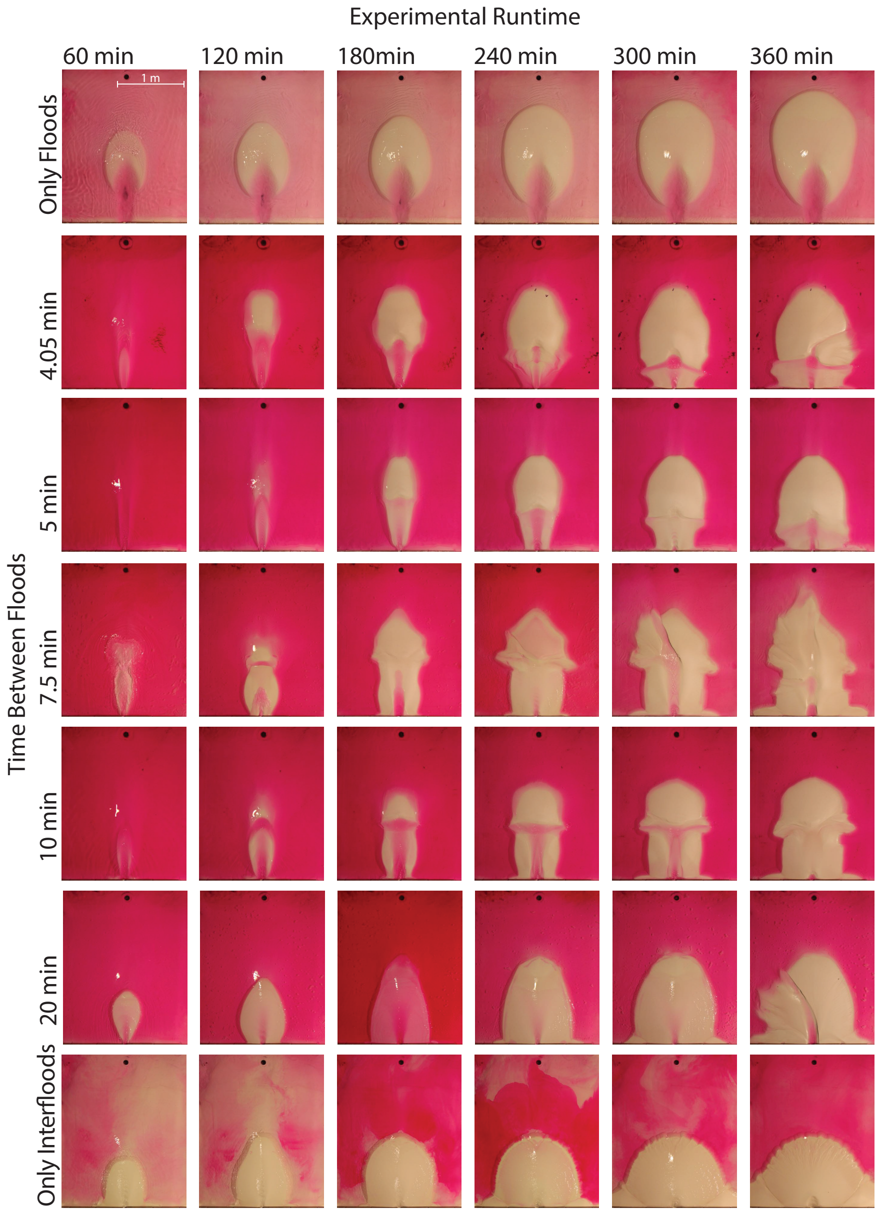

Figure 2.5: A selected ensemble of experimental time lapse photos. Each row is a time lapse of a single experiment. A broad range of morphologies are possible given the same sediment and water mass input. The only changing variable in these experiments is the frequency of flooding. The time between floods increases by row, ranging from only flood discharge, to only interflood discharge. Each column is an overhead photo taken at one-hour increments.

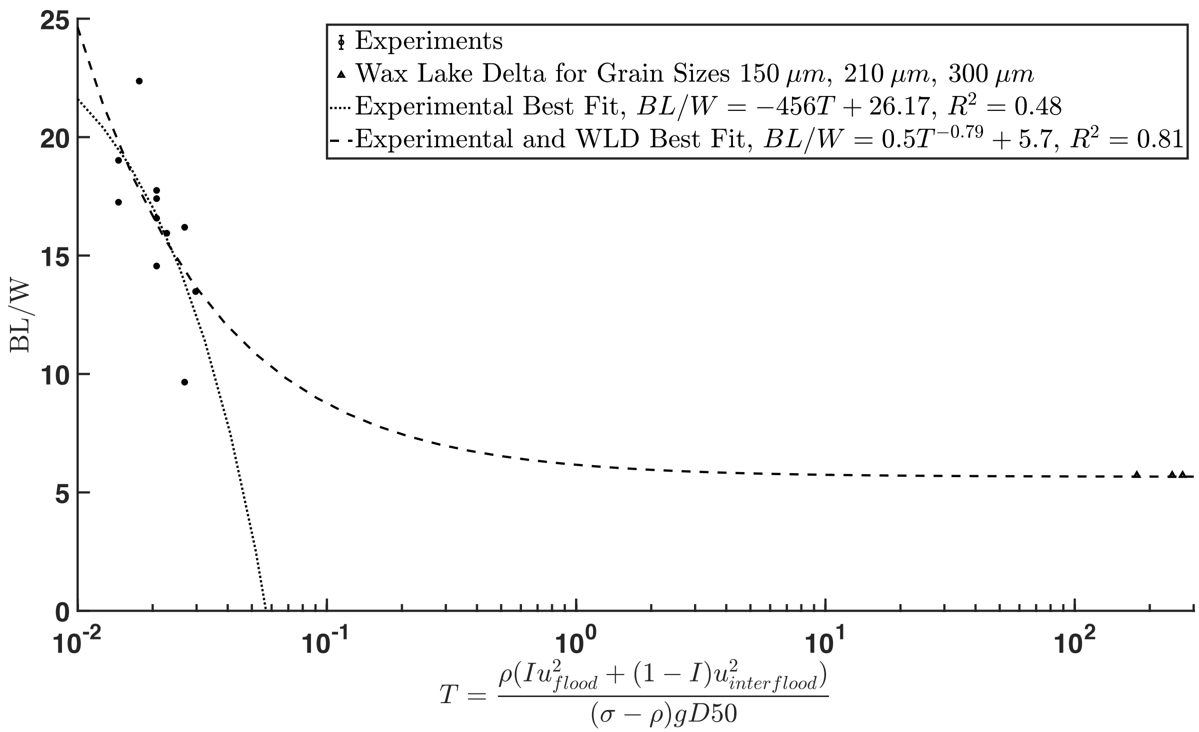

Figure 2.6: Bifurcation length as a function of non-dimensional shear stress, normalized by relative time flooding to interflood flow. Frequently flooding systems have shorter bifurcation lengths than those that flood infrequently. The Wax Lake Delta is included (see supplemental script for determining T).

Chapter 3

Wave-Signal Entrainment Into Combined Flows: Consequences For Sediment Transport, Signal Dislocation, And Turbulence

Author's note: as of this writing, some of the work in this chapter have been published by The Journal of Sedimentary Research. *The paper is published as,* "Experimental Investigations Of Combined Flow Sediment Transport," *by Everett Smith, Max S. Daniller-Varghese, Paul M. Myrow, and David Mohrig.*

3.1 Introduction

3.1.1 Background

In this chapter, I explore the effects of a sediment laden turbulent flow interacting with an imposed wave field. I experimentally modeled the generation of a sediment-laden hyperpycnal flow and track it from a shallow to deep water domain. Persistent turbidity currents like hyperpycnal flows that pass through a wave field have the potential to be strongly influenced by wave energy in a way that persists even after the flow has left the wave field. However, stratigraphy interpreted to be deposited by hyperpycnal flows that contain wave signals, determined by the symmetry of the rippled deposits, are assumed to have been deposited within the so called, "wave base," (Dingler and Inman, 1976). The zone with sufficiently shallow water where the subaqueous sediment surface is subject to wave energy in fair-weather or storm conditions.

Previous work proposed that a turbidity current passing through a wave field could have enhanced ability to transport sediment which would increase flow duration and downstream flux of sediment (Wright et al., 1991; Myrow and Southard, 1996; Myrow et al., 2002). Observations of enhanced sediment transport by naturally occurring wave-supported fluidized mud flows strongly supports this idea (Ma et al., 2010). Although there is previous work experimentally investigating the general dynamics of hyperpycnal flows and their deposits (Lamb et al., 2010), there has been little experimental work concerning the effects of waves on turbidity currents. Field studies have been conducted on wave-supported gravity flows produced in the ocean by ambient waves and currents ((Wright et al., 2001; Wright and Friedrichs, 2006)), and a number of theoretical and numerical modeling studies have addressed such flows (Traykovski et al., 2007; White and Helfrich, 2008; Kämpf and Myrow, 2014, 2018). However, these studies examined wave-modified fluid mud suspensions, not flows with granular sediment, such as the silt-grade sediment used in this study.

Given how likely it is that surface gravity waves affect hyperpycnal flows, and geologic evidence supporting it (Mulder et al., 2003; Myrow et al., 2002; Zavala et al., 2006; Lamb et al., 2008), experimental work on turbidity currents combined with waves are essential. Studying these types of flows enables us to understand the links between the terrestrial and marine realms, including accurate modeling of sediment budgets (Walsh and Nittrouer, 2009). This chapter presents the results of novel experiments that investigate the role that surface waves have on the sediment transport of low-concentration turbidity currents. I demonstrate that under such conditions, surface waves influence the mixing structure of these, "combined flows," and the quantity of sediment transported downslope by such currents.

Laboratory experiments ((Sequeiros, 2012; Smith et al., 2019), Table 3.1), and mathematical modeling ((Liapidevskii et al., 2018)) have both been highly successful tools for investigating many aspects of turbidity currents. Consequently, these flows have a rich literature surrounding them (Kneller and Buckee, 2000; Parsons et al., 2007). Additionally, extensive laboratory experiments and mathematical models have explored the fluid dynamics, sediment transport, and bedforms of oscillatory flows (Wiberg and Harris, 1994; Nienhuis et al., 2014; Perron et al., 2018; **?**; Pedocchi and Garcia, 2009), Pedocchi and Garcia 2009).

Early attempts to construct a combined-flow phase diagram of ripples as a result of the relative input of the unidirectional and oscillatory velocity components by Myrow and Southard, was supplanted by extensive experimental studies by (Perillo et al., 2014,?). Perillo et al. produced phase diagrams for bedforms generated by a wide range of combinations of magnitudes of oscillatory and unidirectional flow components. In terms of combined flows with oscillatory flow and turbidity current flow components, **?** developed a mathematical model for predicting conditions of sediment bypass by wave-supported sediment gravity flows. They corroborated the accuracy of this model with field observations of wave-supported, high density, mud-rich flows (Jaramillo et al., 2009). Aside from a publication on the oceanic dispersal of fly ash (Foster and Stone, 1963), there is little published data on the experiments of wave-modified granular turbidity currents. Our experimental work on the dynamics of combined flows is a significant advance for combined flows, which likely play a major role in sediment transport on modern shelves and played a similar role in the past. In addition, given that much of the field and theoretical work has been done on fluid mud and related deposits, our study of granular sediment is of great significance to the interpretation of silt-grade to sand-grade tempestites in the rock record.

3.1.2 Objectives

In this paper, I report the effects of wave fields on turbidity current sediment transport, and the effect of waves on the dynamics of currents' mixing. My questions are as follows: what effect does the presence of a wave field have on current-driven sediment transport; do combined flows have an increase in bulk downslope sediment transport? Are surface velocity signals transported beneath wave base (Figure 3.1)? What is the mechanism of waves influencing currents? If wave signals in flow are transported from the surface to beneath wave base, then previously interpreted outcrops that define wave base as the location of combined-flow symmetrical ripples must be reassessed (Figure 3.2).

3.2 Methods

The experiments were conducted in the Experimental Sedimentology Laboratory at the Jackson School of Geosciences, The University of Texas at Austin (Figure 3.3). The flume was 11.00 m long, 0.61 m wide, and 1.22 m deep with a ramp constructed inside. At the flume's upstream end (0 m) at an elevation 1.01 m above the base of the flume, the ramp was a horizontal surface from $0 - 1.24\,m$. Beginning at $1.24\,m$, the ramp sloped down the tank at 9° for $5\,m$. It leveled out to a $2.35\,m$ horizontal plane with an elevation $0.06\,m$ above the flume base. While the overall slope of the ramp was constructed at 9°, one of the plates has a slightly lower slope of 7° from 4.88 to $6.00\,m$. The ramp was constructed of $0.02\,m$ thick, $1.22\,m$ long acrylic plastic plates, with a lightly textured, $3\,mm$ thick, rubber mat glued on top for roughness. Beyond the experimental domain there was a sump from $10.00\,m$ to $11.00\,m$, with an added depth of $0.73\,m$ beneath the flume bottom connected to a drain. The sump included a standpipe to maintain constant water depth $1.15\,m$ above the true flume bed during experimental flows. The wave field was generated with a $2' \times 4'$ ($0.6\,m \times 1.2\,m$) acryllic plastic paddle fixed on a drive shaft attached to a motorized wheel, submerged approximately $0.1\,m$ into the water. A foam mat in the upstream end of the flume reduced reflections off the back wall. The wave maker generated waves with a $0.013\,m$ amplitude, an approximate $3\,m$ wavelength, and a period of $1.4\,s$.

Each flow was composed of $900\,l$ of water mixed with $113.4\,kg$ of 200 mesh quartz silt ($D_{50} = 30\mu m$) in a 1000 liter reservoir creating a 942 liter mixture of 4.5% percent quartz silt concentration by volume. This mixture was pumped to a constant head tank feeding the flume through a $51mm$ diameter PVC pipe flush with the ramp. For the duration of each flow, augurs continuously mixed the sediment and water in both the reservoir and head tank.

A Nortek Vectrino Profiling Velocimeter (PV) measured flow velocity at the centerline of the flume at $8.31\,m$ from the rear of the flume. The PV measured the flow in 2 mm vertical bins between 3 mm and 73 mm above the bed, at a frequency of 10 Hz (Figure 3.3). Among the total of 9 experiments, experiment 9 had a second PV probe near the inlet. In experiments 1 and 2, the PV took velocity measurements from 92.6 mm to 120.2 mm with 2.0 mm spaced bins and 63.9 mm to 106.7 mm with 2.0 mm spaced bins, while in every other experiment the PV took data from 0 to 28 mm above the ramp with 2.0 mm spaced bins. A Keyence laser altimeter on a moving carriage measured centerline elevation from 8.03 m to 4.73 m. A Nortek Aquadopp Acoustic Doppler Profiler (ADP) mounted to the front of the carriage collected velocity measurements at 4 or 8 Hz, depending on the experiment, over the entire water column, excluding a blanking distance of 100 mm. The profiler was mounted orthogonally to the ramp, and used one transceiver, oriented 25° off the ADP longitudinal axis, directed downslope. The horizontal and vertical components of the measured velocities in the reference frame of the ramp were resolvable as ($u = Ucos(25°)$, $w = Usin(25°)$). The ADP data was collected in 25 or 30 mm vertical bins.

The ADP velocity data was filtered using a rule-based system. One return from the instrument was correlation-of-signal-return at each bin for each measurement. I masked all the data that fell beneath a threshold of 70%. I then removed the upper and lower tenth percentile of data within each bin to remove more spurious values. Lastly, I applied a rule that if more than 50% of the data had been filtered from a given bin, then the bin was categorized as unreliable, and its data was ignored.

The primary variables are the presence or absence of the imposed wave field, the inlet discharge of the current (either 1.25 l/s or 0.6 l/s), and the position of the inlet (either $x = 1.3\,m$ or $4.3\,m$) in the tank. All of these were used to test the relative effects of a wave field on a current. I ran 9 experiments in total, hereafter referred to as experiments 1 though 9 (Table 3.1). Experiments 5-8 were the same as experiments 1-4, but had a higher inlet location in the flume located 1.3 meters from the rear versus 4.3 meters (Figure 3.6). These are referred to as the, "long domain," and "short domain," respectively. Experiment 9 has an additional, identical profiling PV mounted in the center of the flume at location $3.18\,m$ in the center of the flume (Figure 3.3), which was used to take velocity measurements with the purpose of creating simultaneous time series data for both upslope and downslope locations.

3.2.1 The Imposed Wave Field

The orbital velocities of gravity waves decay exponentially with depth (Figure 3.4) ((Holthuijsen, 2007), after (Airy, Airy)). In our experiments, near-surface orbital wave velocity root-mean-square was $0.015\,m/s$, and it decayed to near zero at the base of the ramp ($u_{rms} = \sqrt{\frac{1}{N}\sum_{n=1}^{N}|u(n)|^2}$). This profile fits an exponential decay relationship with depth:

$$u(z) = ce^{-kz}, \tag{3.1}$$

where c is a near-surface wave orbital velocity ($0.015\,m/s$ for the RMS field), z is depth beneath water surface, and k equals 2π divided by the wavelength at the surface, $3\,m$. The surface waves have the same velocity across the tank, and the magnitude decays with depth. The rate of decay is different from upstream to downstream. Upstream (e.g., 5 and $5.5\,m$) there is only minimal decrease in velocity with depth, but much more in the more distal positions. Overall, the root-mean-squares of the measured velocity profile time series correspond with the predicted decay ($R^2 = 0.71$). Reflections at the upslope region of the tank, which diminished with increasing water depth, may have altered the oscillatory field but only to a minor degree. To compare our experiments geometrically to a modern shelf: a $0.1\,m$ thick current moving through waves of $0.01\,m$ amplitude in $1\,m$ of water, is approximately equivalent to a $10\,m$ thick current in a wave field with surface amplitudes of $1\,m$ in $100\,m$ deep water. These are realistic conditions for storms on modern shelves.

3.3 Results

3.3.1 Grain Size

After the long domain experiments were complete, I took grain size samples at half-meter intervals along the tank centerline (Figure 3.5). One can observe the median grain size decreases downslope, and the sorting improves. However, there is very little difference in the grain size distributions of the deposits when comparing a combined flow and its corresponding turbidity current only experiments (Figure 3.5). The primary difference in grain size distribution is a function of the inlet discharge, where high discharge cases have coarser sediments in the sampled domain, while lower discharge cases have finer sediments in the sampled domain (Figure 3.5).

3.3.2 Sediment transport

I recorded the centerline elevations after each run on the medial portion of the deposits (Figure 3.6). By taking the cumulative sum of the deposit thickness and normalizing it with the total thickness, I were able to determine the spatial accumulation of each deposit.

$$CS(\eta, x) = \frac{\sum_{4.3}^{x} \eta(x)}{\sum_{4.3}^{8.0} \eta}, \tag{3.2}$$

where $\eta(x)$ is the accumulation profile at x ranging from $x = 4.3\,m$ to $x = 8.0\,m$. This method allows us to examine the bulk distribution of sediment in the deposit, determining the center of deposition volume of each run in our scanner domain. I found that combined flows' deposits have a downslope shift in their center of volume relative to a turbidity current, on average, 8% in the short domain runs (experiments 1 through 4) (Figure 3.5). In the long domain runs (runs 5-8), the low flow cases had a 2% difference, and the high flow cases had a 4% shift. While the downslope shift in bulk sediment mass changes in magnitude depending on the input velocity relative to the wave field, in both high and low flow cases, there is a downslope shift in sediment transport with the presence of a wave field.

Two limitations of the elevation-measuring apparatus are the blanking distance from the head, and the length of the rails on the flume. The blanking distance prevents scans at the proximal-most end of the tank, and the length of the rails limits the scans to a subdomain within the flume. I expect that if the laser altimeter had a shorter blanking distance, and the carriage were able to scan the entire deposit, the differences between combined flow deposits and their counterparts without waves would be shown in starker relief.

3.3.3 Combined Flow Wave Signal Velocity

To test whether the wave signal within the body of combined flows is the same as that of the wave field, I compare the velocities of the two signals. The velocities of the wave signal were extracted from the data with a fifth-order Butterworth bandpass filter with a band ranging from 0.67 Hz and 0.83 Hz (Figure 3.5). I find the wave signal velocities within a combined flow, the filtered components I extracted, are greater than the measured values from the imposed wave field without a current (Figure 3.8). A two-sample Kolmogorov-Smirnov (K-S) nonparametric test determines the degree to which two samples of data are likely to have been taken from the same distribution (Massey, 1951). By examining the difference between the two samples, and applying a significance level α, I can assert a level beyond which the samples cannot be distinguished as coming from distinct populations. I applied this test to our data and found that it rejects this null hypothesis. The wave signal sampled from the combined flow and that sampled from the wave field alone are not from the same distribution with a significance level of $\alpha = 0.05$ and a high degree of certainty, $p << 0.01$ in all experiments except experiment 5 (a low flow combined flow in the long domain) where $p = 0.031$ (95% confidence for p values < 0.05). In all of these cases, the wave signal within combined flows is statistically distinct from the observed wave signal from the wave field at that location.

3.3.4 Direct Measurements of Turbulent Kinetic Energy

The turbulence of the flows is quantified by a dimensionaless turbulent kinetic energy (TKE), which is a function of the deviatoric velocity fluctuations.

$$TKE = \frac{\frac{1}{2}(u'^2 + v'^2 + w'^2)}{\overline{u}^2}, \tag{3.3}$$

with u', v',and w' representing instantaneous velocity fluctuations from the mean velocity in the bed-parallel orientation in the horizontal, cross stream, and vertical directions, after the known periodic component associated with the wave field has been filtered, $u' = \overline{|u(t) - \overline{u}|}$. This value is scaled against the mean horizontal velocity squared, $\overline{u}^2$.

The TKE of each flow was calculated over a 60 s duration, and scaled by the mean velocity of the profile in the downstream direction, $\overline{u}$, in the body of flows with and without waves. In these experiments, the mean-velocity scaled TKE in the current body is lower in combined flows than in their corresponding turbidity current without waves (Figure 3.9). The exception to this trend are the experiments 3 and 4, low flow in a short domain. Experiment 3, which had waves, has higher TKE is higher than the experiment without waves, experiment 4.

Comparing the experiments, in low flow in a short domain, (experiment 3 relative to 4), the combined flow has 72% more TKE. In low flow with a long domain, (experiment 5 relative to 8), the combined flow has 54% the TKE of the current without waves. In high flow in a long domain (experiment 7 and 6) the combined flow has 86% the TKE of the current without waves. Experiments 1 and 2, high flow in a short domain, measured the TKE higher up in the column at the interface between the currents and the ambient fluid, ranging from 80 mm to 120 mm above the ramp. In this case, the combined flow has 3.6 times the TKE of the current without waves. The presence of waves correlates with suppressed TKE in the body of the currents in the cases where the domain was long, and the inlet was nearer to the surface. In these cases the bodies of combined flows are generally less turbulent than turbidity currents (Table 3.1). However, in the cases of the small domain with a deeper inlet, experiments 1, 2, 3, and 4, The presence of waves has the opposite effect: combined flows are more turbulent than their counterparts.

3.4 Discussion

Briefly summarizing our observations, combined flows have increased downslope transport relative to a turbidity current without waves (Figure 3.6). Grain size recorded in our experiments' deposits is a function of flow magnitude, rather than the wave field. Next, I observed that the wave signal filtered from combined flows had a greater magnitude than the signal from a wave field alone at the same depth. Lastly, I calculated the turbulent kinetic energy, TKE. I found that my long-domain experiments, where currents interact with a stronger wave field than their short-domain counterparts, combined flows typically had a suppressed turbulent profile relative to their corresponding experiment without waves. However, in the cases with a deeper inlet, combined flows were more turbulent.

Revisiting our questions from the Objectives section. What effect does the presence of a wave field have on current-driven sediment transport? Combined flows have a net increase in downslope transport (Figure 3.6). Are surface velocity signals transported beneath wave base? The wave velocity signals within combined flows are statistically distinct from those of a wave field without a flow (Figure 3.8). What is the mechanism of waves influencing currents? To answer the final question, I present a model framework that encompasses all our observations.

3.4.1 How do Surface Waves Combine with Currents?

One possibility for wave-signal entrainment into the body of a current are direct, overhead influence where the wave signal impinges into the body of the current completely as an additive to the mean field (Inman, 1957; Dingler and Inman, 1976). Under this conceptual framework, the wave velocities would add or subtract from the current velocity. The wave signal inside the body of a combined flow would be exactly the same magnitude as the signal I measured in the wave field without a current. I can discount this because as already demonstrated in the results section (Figure 3.8), the wave signal I observe in the body of the current is stronger and quantitatively distinct than the ambient wave field without a current.

Another option is that the wave field fundamentally affects the dynamics of the current itself, changing the mixing within the current and its interactions with ambient fluid. The wave signal becomes a periodic mixing component within the body of the current. In this case, the combined flows' turbulent structure would be different from a current without waves. This possibility already has some evidence supporting it, based on the measured differences of TKE in the combined flow body relative to a current with no imposed wave field (see Results, Table 3.1, Figure 3.9). It follows that differences in turbulent structure and imposed periodicity would lead to differences in how combined flows mix with ambient fluid.

By examining the area directly above the body of the current, approximately $0.1\,m$ above the ramp, I determine whether the presence of waves disrupts currents' characteristic mixing. If the Kelvin-Helmholz circulation cell, which is the primary mechanism of ambient fluid entrainment and dissipation of momentum of a current

(Simpson, 1997; Baas et al., 2005), is suppressed then I can conclude that the presence of waves leads to mixing suppression. I propose that the mechanism of entrainment is caused by direct forcing of the current by the wave field in the near surface. This induces a periodic component of mixing within the body of the current. The wave field disrupts the Kelvin-Helmholtz circulation cell, preventing the entrainment of ambient fluid into the current and suppressing mixing between the current and ambient fluid. Because mixing is suppressed, the wave signal from the near surface is preserved within the body of the current as it transports downslope.

3.4.2 Mixing at the Boundary with an Eddy Viscosity Model

I present a framework for understanding how wave signals entrain into a turbidity current to create a combined flow, and examine how this process can suppress turbulence. Using eddy viscosity, I can characterize the degree of mixing with a single parameter. The eddy viscosity, ν, is a characteristic of a flow that compares the turbulent stress against the shear from the mean velocity field (Starr, 1968). A high eddy viscosity implies a large degree of turbulent stress relative to shear; the column mixes effectively. A low eddy viscosity implies a large degree of shear relative to turbulent stress; the current does not mix effectively. Eddy viscosity is described by the following:

$$\nu = \tau_R / \frac{\partial [u]}{\partial z} \tag{3.4}$$

Where τ_R is a turbulent stress component, and $[u]$ is the mean velocity within a binned elevation:

$$[u] = \frac{1}{L} \int_{x_1 - L/2}^{x_1 - L/2} u dx \tag{3.5}$$

where L is a length parallel to the x axis, centered at point $x = x_1$. Numerically, eddy viscosity can be expressed as:

$$\nu(z) = \overline{u'w'}/\frac{u_{z-1} - u_z}{\Delta z} \tag{3.6}$$

where u is the horizontal component of velocity, $\Delta z = z_0 - z_1$ is the length of each measured bin, and $u' = \overline{|u(t) - \overline{u}|}$, the average fluctuation away from the mean (Figure 3.12), with the periodic component filtered out of the time series, using the filter described in the Methods section. The temporal component of eddy viscosity is the Reynolds stress in the downstream direction, $(\overline{u'w'})$. It represents average turbulent stress at each depth bin. The spatial velocity gradient is the degree of shear within the column. By using the Profiler data (Figure 3.10) comparing the turbulent stress against shear in the column, I can understand how vigorously the column mixes its velocity components (Figure 3.11 and Figure 3.12). Recall that high eddy viscosity values indicated that the column is mixed more effectively relative to low eddy viscosities.

For comparability within the flume and each experiment, depth is scaled by the thickness of the current and the height of the current core, after Altinakar et al. (1996):

$$scaled\ depth = 1 + \frac{z - h_m}{h - h_m} \tag{3.7}$$

with z as the unscaled depth, h_m as the height of maximum velocity in the current, and h as the thickness of the current.

3.4.2.1 Mixing with the inlet in shallow water

Comparing the eddy viscosities between experiments with waves, experiment 7, and without waves, experiment 6, in the long domain at high discharge, I observe the eddy viscosity in both cases to increase directly above the body of the current, indicating a large degree of shear relative to the ambient fluid (Figure 3.13). The eddy viscosity then decreases higher up in the column. Directly above the body of the two currents, the combined flow (experiment 7), has a lower eddy viscosity, indicating that mixing is being suppressed in that layer, where the current interfaces with ambient fluid. By suppressing mixing between the current and the ambient fluid, the current's mean field is enhanced relative to turbulence, allowing for greater downslope transport of sediment.

I observe that mixing between the core of the current and the overlying current is suppressed in the combined flow cases (Figure 3.13). Mixing is disrupted in the presence of a wave field, reducing the dissipation of momentum from the current to the ambient fluid. This explains the reduced TKE profiles within the body of the combined flows measured at the downslope end of the tank (Figure 3.9). This also explains the wave signal strength carried within the body of the current. If momentum dissipation is suppressed in combined flows, then the wave signal that the current takes on as a periodic component of mixing will also not be diffused into the overlying fluid. Rather than decelerating like the current without waves, it maintains its velocity, which allows it to transport sediment further downslope.

The low flow experiments in the long domain pose a slightly more difficult conceptual framework. Experiments 5 and 8, the long domain experiments, have little difference in their bulk downslope sediment transport, with their center of volume being within 2% of one another. If I examine the eddy viscosities (Figure 3.14), I observe there is no substantive difference in their values within the body of the current or directly above it in the mixing layer. However, I do observe waves' effect in other ways; the combined flow (experiment 5) does carry a stronger wave signal than expected (Figure 3.8), and the turbulence inside the combined flow is suppressed (Figure 3.9). In this case, because of the length of the domain and the weakness of the current, the effects of the waves are not substantial enough to affect the sediment transport. While the current's dynamics are affected, the overall stratigraphic signature is negligible. I propose that while there is wave-signal entrainment, the weakness of the current is the most salient control, where the currents' deceleration has a larger effect on its internal dynamics than the wave field. This is borne out by the similar mean velocity profiles of the two experiments (Table 3.1).

3.4.2.2 Mixing with the inlet in deeper water

In deeper water, in the short domain experiments, the mixing effects I observed in the long domain are reversed. These combined flows are more turbulent than their counterparts without waves, though there is still enhanced sediment transport, 7-8.5% in the high and low flow cases (Figure 3.6). Focusing on the low flow cases, experiments 3 and 4, there appears to be little difference in the eddy viscosity profiles within the current, and some suppression of mixing directly above the current body for the turbidity current, though the values overlap substantially. This correlates with the slightly more turbulent profile observed within the current in Figure 3.9. Because the inlet location is located in deeper water, the wave energy at the combined flow as it enters the flume is weaker, and is able to effect the dynamics of mixing less effectively than those currents that initiated in shallow water.

Because sampling frequency for experiment 1 and 2, the high flow experiments in the short domain, was 4 Hz rather than 8 Hz, like in the other experiments, I do not report the eddy viscosity. The turbulent stress term is inadequately characterized at that frequency.

3.4.3 Reynolds Stress and Sediment Transport in Combined Flows

In the case of low flow, in a short domain, I am presented with seemingly contradictory results. Experiment 3, the combined flow, has increased downslope sediment transport, but a similar mean velocity profile as the current without waves (Figure 3.1). It carries a strong wave signal (Figure 3.8), but it has a greater measured TKE within its body (Figure 3.9). The eddy viscosity profiles are indeterminate when compared with experiment 4, with sub-equal values above the body of the current (Figure 3.15). These experiments must represent a different process of wave-signal influence on currents.

Because these experiments have a shorter domain in deeper water, the wave field is able to affect the current, but not as substantially as a currents initiated in shallow water. Waves influence the upper part of the current and the mixing layer, but the effect is not strong enough to affect the turbulence within the body of the current itself. That, in turn, creates a combined flow that has more turbulent kinetic energy within its body. One would expect that a more turbulent flow would result in less downslope transport, but that is not the case in these experiments.

The Reynolds shear stress ($\tau_R = \overline{u'w'}$) of the flows offer some insight (Figure 3.16). The Reynolds shear stress quantifies the turbulent stress in the downstream and upward directions. In the long domain experiments the measured Reynolds shear stress in the current body is weaker than in the combined flows than their corresponding currents. In addition, the vertical component of turbulence, w', is suppressed in combined flows (Figure 3.17). In contrast, Experiment 3 also has enhanced vertically directed turbulent stress. In experiment 3 TKE is high because of the enhanced vertically directed turbulent stress, which increases turbulent shear. In this case the bulk shift in sediment transport is due to the enhanced stress associated with turbulence re-suspending sediment, rather than more energy in the mean field.

3.5 Conclusions

Understanding how surface waves modify turbidity currents, and how those combined flows evolve in space is important for interpreting tempestites and modeling the sediment budgets on continental shelves. Our first question was whether the presence of waves affected the depositional signal of a turbidity current. I found that combined flows typically had greater net downslope transport of sediment (Figure 3.6). In our experiments, the wave velocities were an order of magnitude smaller than downslope current velocities. I speculate that a stronger wave field would result in stronger pulsation or even reversing flows. This could result in a profound increase in downstream sediment transport, which has important consequences for shallow marine storm deposition.

The next question was whether surface wave velocity signals transported beneath wave base. The experiments showed that wave velocities inside combined flows are stronger and have distributions distinct from the expected local wave velocity (Figure 3.8). This indicates that the wave signals are transmitted from upslope to downslope within the body of the current as a periodic component of mixing. In all experiments, the extracted wave signal was found to be distinct from the expected wave signal magnitude. This increase in oscillatory velocities must result from a transfer of momentum from shallow depths where surface wave influence is higher. This transfer may result from oscillations at the interface of the turbidity current and the overlying flow, which occurs more readily in shallow water.

I had two, related final questions. How do waves affect turbidity current mixing, and how do waves entrain themselves into currents? I applied an eddy viscosity model, which quantifies the magnitude of eddy dissipation. At the interface between the combined flow and the ambient fluid in the velocity profiles reveal that combined flows initiated in shallow waters have suppressed mixing at that layer, isolating the current and preventing it from entraining water and depositing its sediment (Figure 3.13). This isolation allows the periodic component of mixing, which is induced in shallow waters where the wave field is strong (Figure 3.4), to be maintained as the current transports downslope. The turbulent kinetic energy measured within the body of these currents indicates the presence of waves suppresses turbulence in combined flows, preventing the dissipation of momentum, and allowing greater downslope transport of sediment. The presence of waves in these experiments correlates with a suppressed time-averaged TKE profile.

However, in the cases where flows initiate in deeper waters, where wave energy interacting with the current is weak, result in a different effect. Mixing is not suppressed at the boundary between the sediment gravity current and the ambient fluid, but the Reynolds shear stress still increases (Figure 3.9). The increase in sediment transport in this case due to turbulent resuspension of sediment, rather than an increase in mean flow velocity.

The experiments show that wave modified turbidity currents should be considered an important process for offshore sediment transport that explain discrepancies between processes and deposits in shallow marine systems. Not only did I determine the effects of a wave field on a turbidity current in the depositional record, but I interrogated the processes at work that allow a current to entrain a wave field and enhance flow capacity. Enhanced flow capacity and altered flow competency with surface wave-modification of turbidity currents needs systematic study across different ratios of oscillatory to unidirectional velocities and over varying slopes, grain sizes, sediment concentrations, and flow rates.

Table 3.1: The three conditions that varied between flows (inlet location, flow release rate, and the presence or absence of surface waves), shown for each flow.

Experiment	Inlet Location	Discharge (l/s)	Surface Waves	Downslope $\overline{u}$, (m/s)	Body $\overline{TKE.}/\overline{u}$, ( )
1	4.3	1.25	Present	3.98e-2	–
2	4.3	1.25	Absent	2.77e-2	–
3	4.3	0.6	Present	2.37e-2	0.030
4	4.3	0.6	Absent	2.17e-2	0.018
5	1.3	0.6	Present	3.25e-2	0.020
8	1.3	0.6	Absent	4.30e-2	0.036
7	1.3	1.25	Present	6.51e-2	0.022
6	1.3	1.25	Absent	3.08e-2	0.025

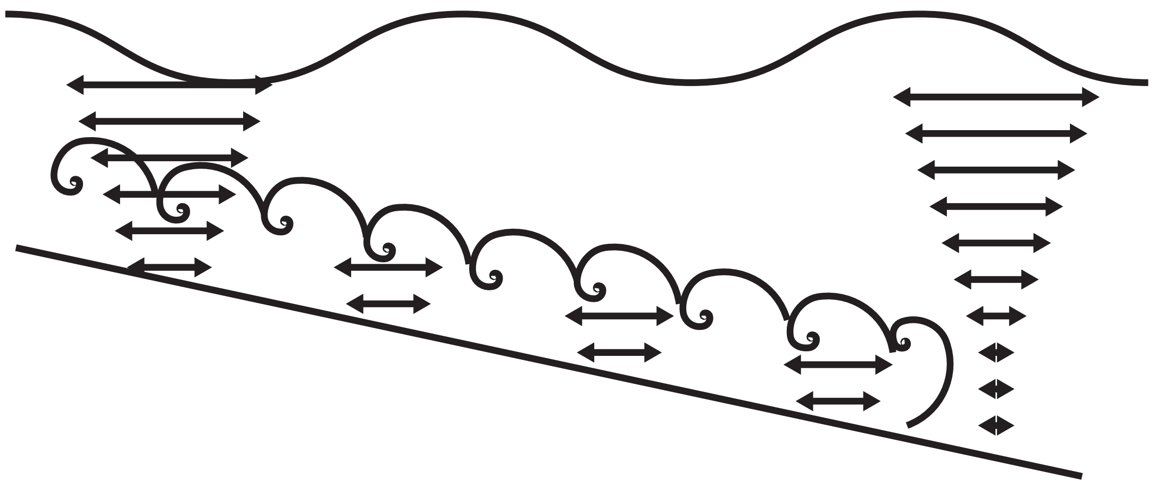

Figure 3.1: A conceptual diagram for a turbidity current entraining a near-shore wave signal, and transmitting it within the current body downslope as a periodic mixing component.

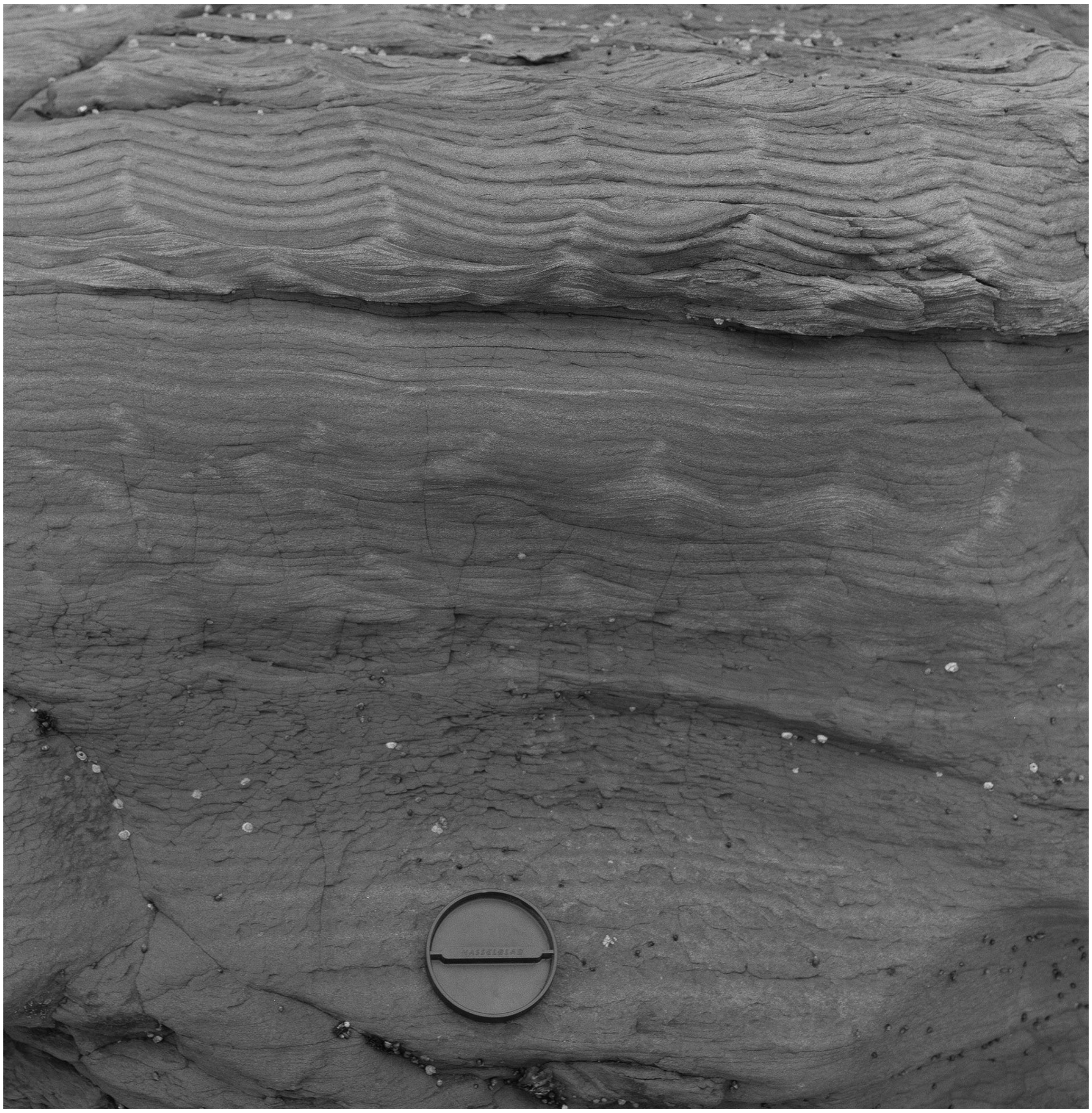

Figure 3.2: An example of combined-flow ripples in outcrop in Coos Bay, Oregon. The deposit is interpreted as the stacked succession of a tidally-influenced combined flow. The light color at the ripple crestline indicates coarse grains at the crestline. Rather than drape over antecedent topography, these represent an active, bidirectional current.

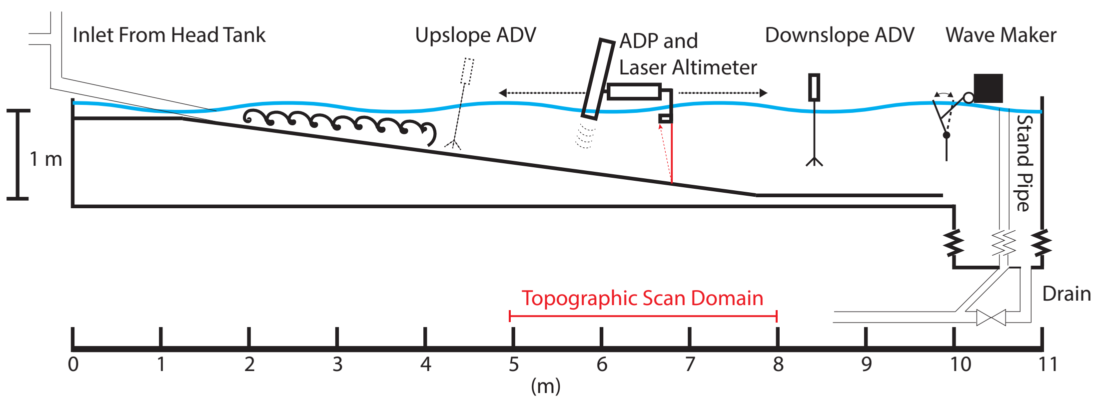

Figure 3.3: A vertically exaggerated schematic of the experimental setup. During flows 1-4, the inlet location is at 4.3 m, and during flows 5-9 the inlet location is 1.3 m. The length and location of the topographic scan domain remained the same for all 9 experimental flows. During flow 9 the downslope Profiling Velocimeter (PV) remained in the same location as experiments 1-8, and another PV was added at the upslope location shown. During flow 9 the Acoustic Doppler Profiler was only used at the upslope location, and during other runs the cart was driven to various locations along the domain.

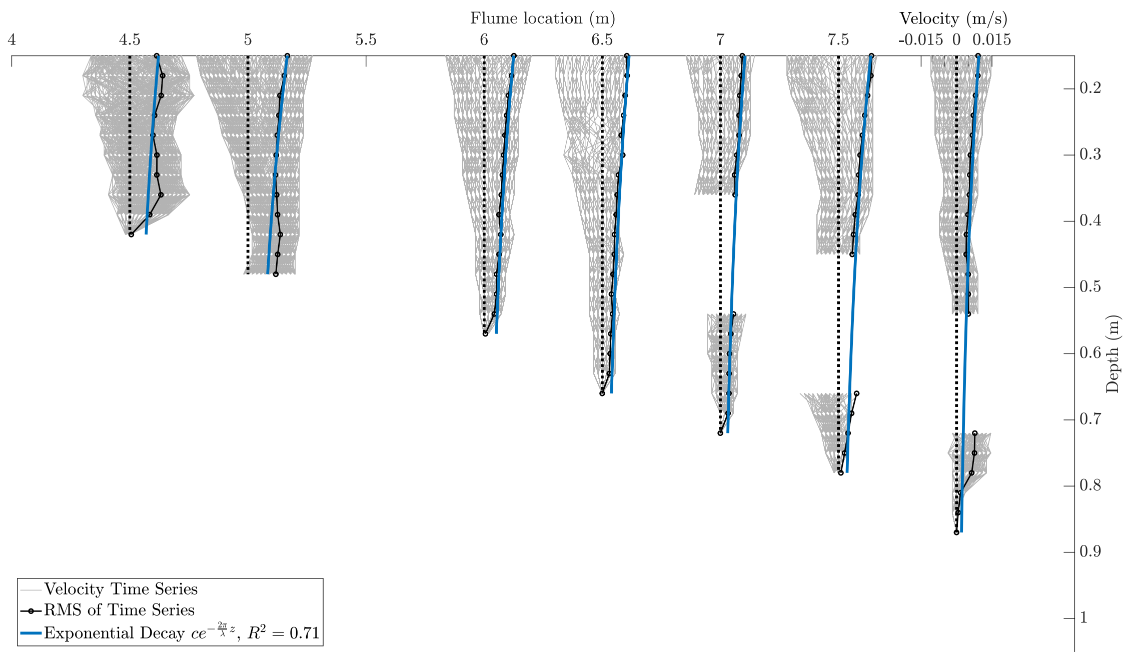

Figure 3.4: The horizontal velocity time series measurements of the wave-field alone measured by the Acoustic Doppler Profiler (ADP). The data are plotted in the flume spatially to give a relative sense of the velocity field. The data has spurious values that were removed using a threshold correlation of the ADP signal return (correlation threshold = 70%) and the filter described in the Methods section. Velocity root-mean-square values are reported with the solid black line with circular markers. Zero axis is the dotted black line. The predicted behavior, exponential decay of the surface velocity (Equation 3.1, (Holthuijsen, 2007), after (Airy, Airy)), is the solid blue line.

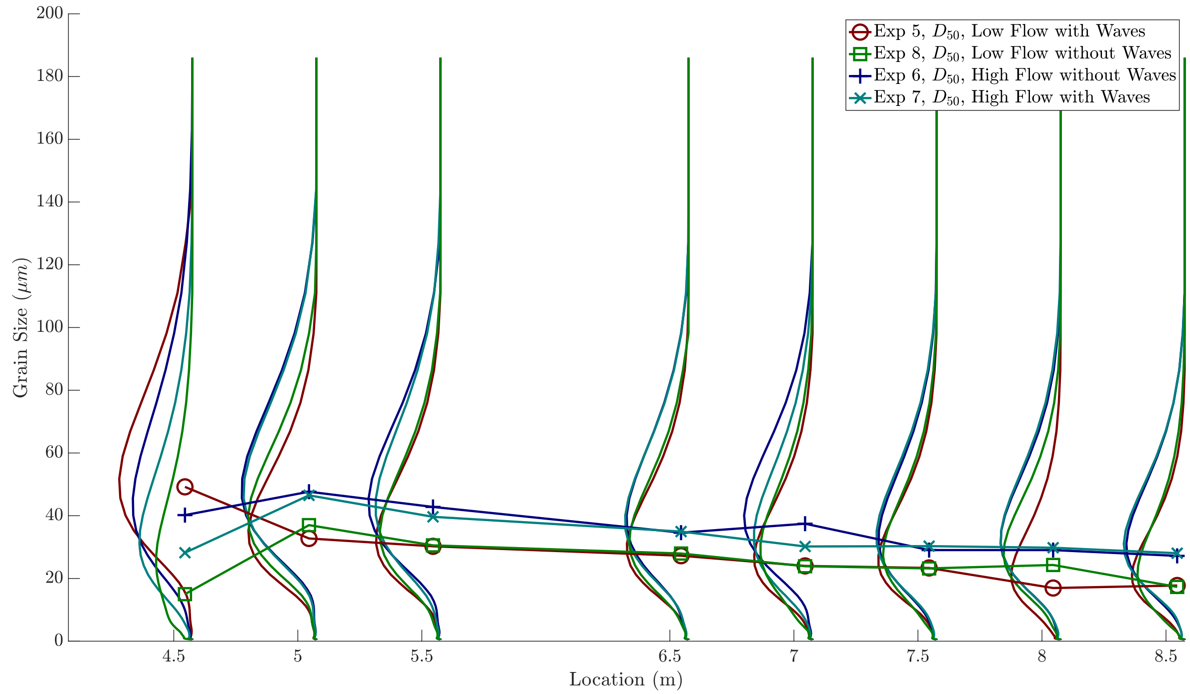

Figure 3.5: A violin plot of the probability density functions and D_{50} measurements for samples collected from the deposits of flows 5-8 (Table 3.1) at the same 8 locations along the flow deposit. Location numbers indicated on the x-axis match locations given in Figure 1 along the flume bed. Upslope is to the left and downslope locations are to the right.

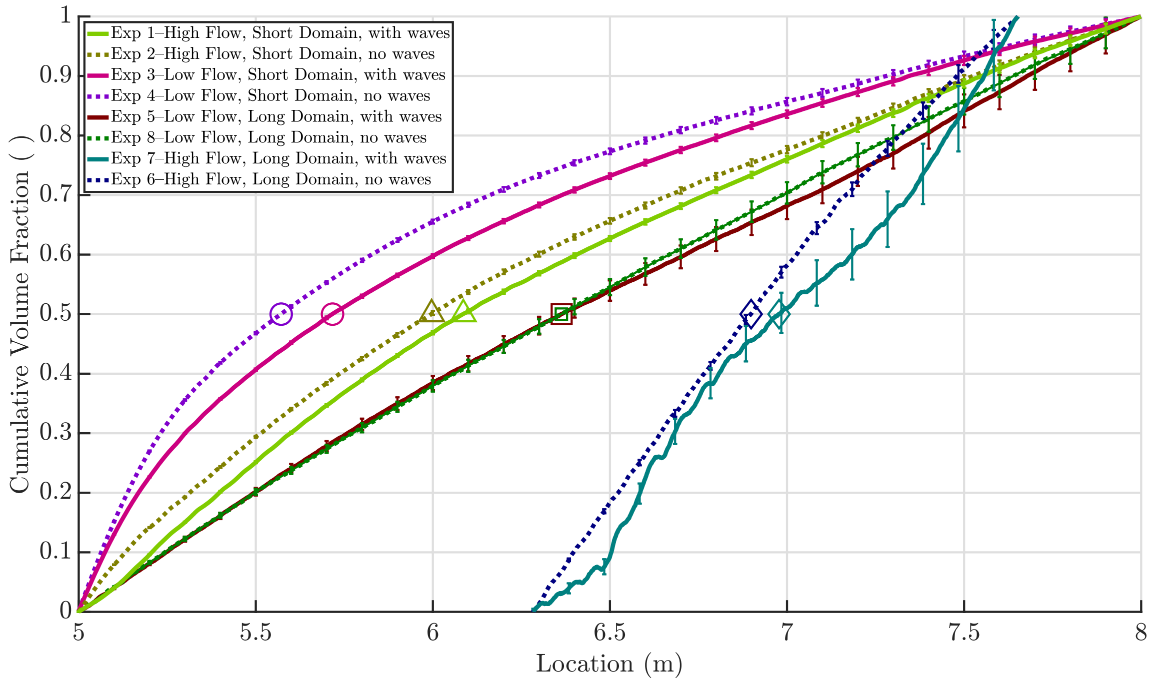

Figure 3.6: The cumulative fraction deposited within the topographic scanner domain for flows 1-8. The upslope end of the flow deposits is located on the right at position, 4.3 m, and the downslope end of the flow, 8 m. In both cases of high and low discharge, wave input increases net downslope transport. Due to an operator error in the initial data acquisition, experiments 6 and 7 are in a subdomain further downslope from 6 m to 7.6 m.

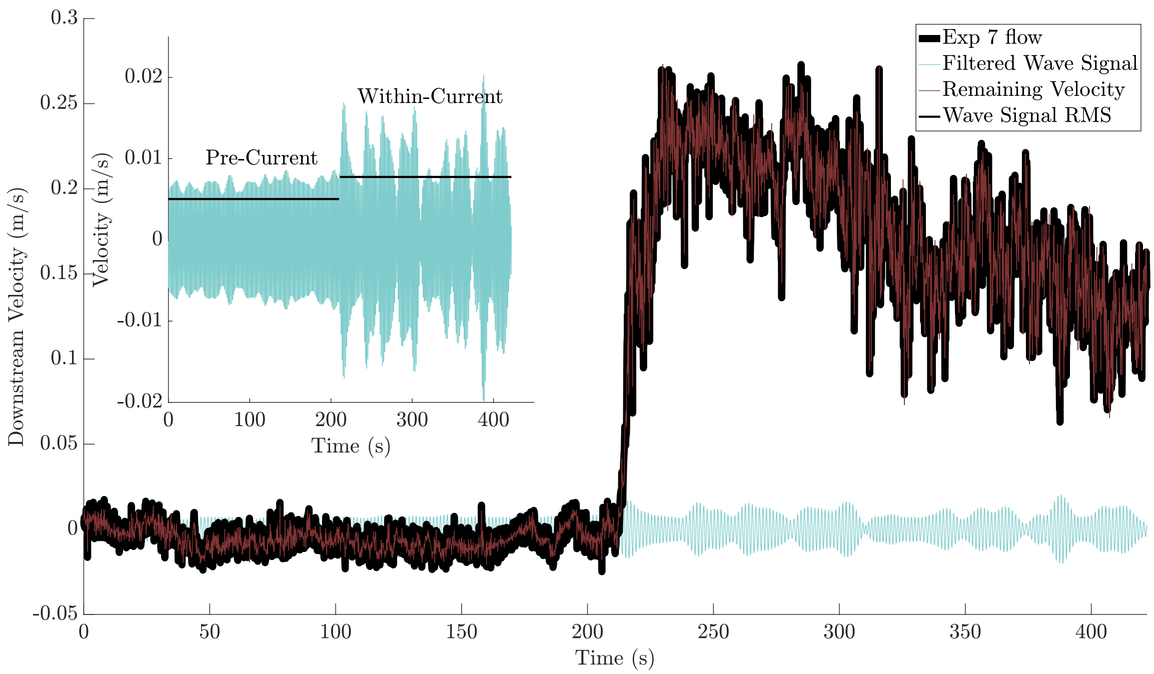

Figure 3.7: The time series measurements from the downslope Profiling Velocimeter (PV) during the wave modified ensemble of flow 7, a high-flow, long-domain experiment, as the head of the combined flow passes under the PV. The wave signal extracted from PV time series using a fifth-order Butterworth bandpass filter, with a frequency range of 0.67 Hz to 0.83 Hz, is shown as the lower oscillatory line. The wave-signal subtracted from the PV time series data is shown as the turbulent red line overlying the initial, thick line, which is the initial data. INSET, The wave velocity data of the larger figure plotted alone. Note the difference in the amplitudes of the wave velocity before the current passes beneath the PV, and the wave signal measured within the current. The root-mean-square of the signal is plotted in the horizontal black lines.

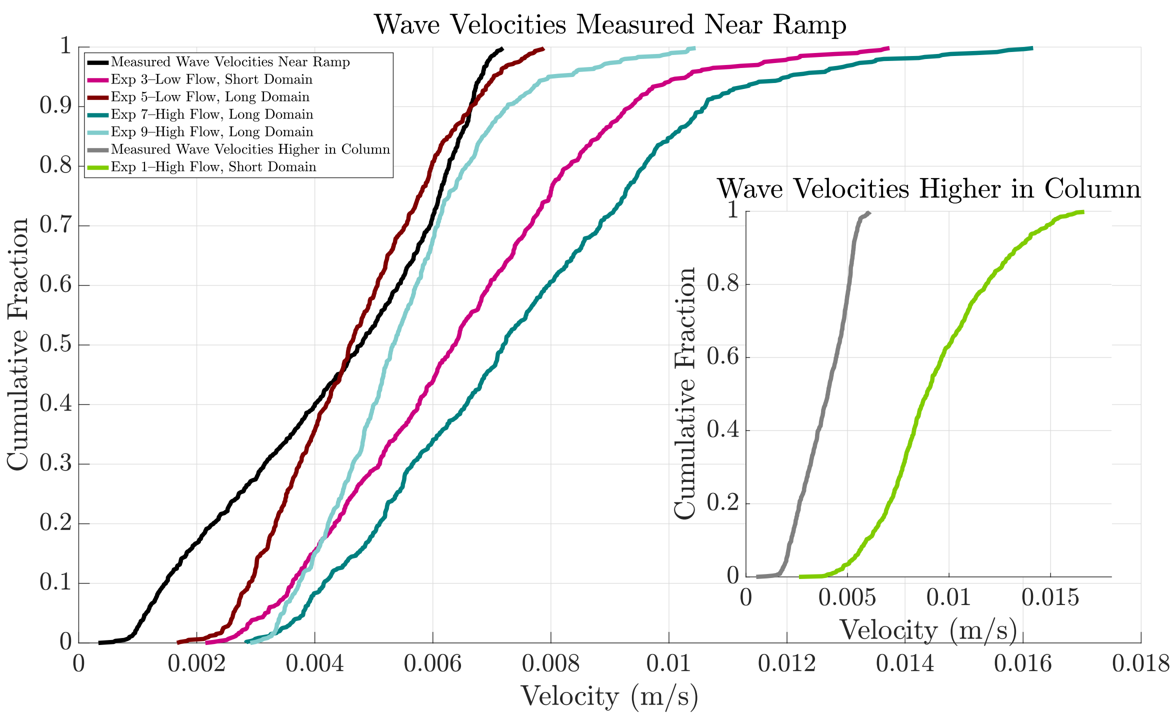

Figure 3.8: Cumulative distribution functions of the extracted wave signal magnitude in velocity profiles from both Profiling Velocimeters. These data were taken at the downstream end of the flume from 0 mm to 30 mm above the ramp (8.31 m from the rear of the flume). These data were taken from 60 seconds of data within the combined flows. A two-parameter Kolmogorov-Smirnov test was used to test the null hypothesis whether the time series are from the same continuous distribution. All the distributions reject the null hypothesis at the 5% significance level with $p < 0.05$. INSET: experiments 1 and 2 measured data from higher in the column (90 mm to 120 mm), and must be assessed independently.

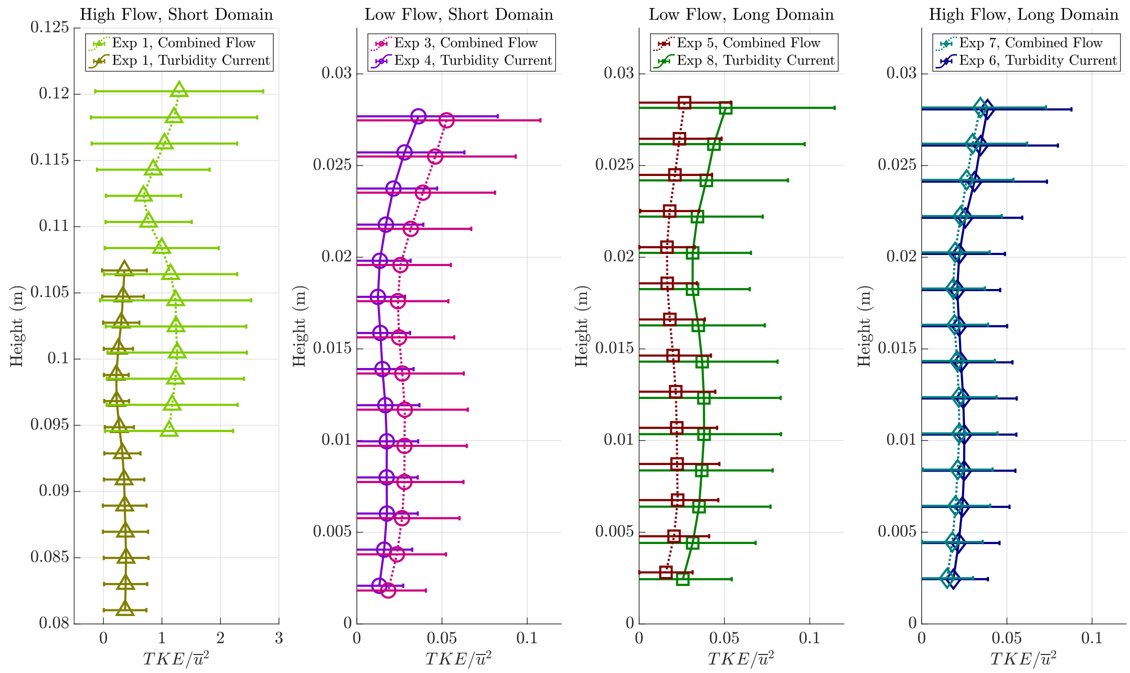

Figure 3.9: Dimensionless Turbulent Kinetic Energy measurements $TKE = \frac{\frac{1}{2}(u'^2+v'^2+w'^2)}{\overline{u}^2}$ as a function of depth. In all experiments except experiments 3 and 4, combined flows have less TKE within their bodies than their corresponding flow without waves. These data were taken at the downstream end of the flume (8.31 m from the rear of the flume) from 0 mm to 30 mm and 90 mm to 120 mm above the ramp. These data were taken at the downstream end of the flume (8.31 m from the rear of the flume) from 0 mm to 30 mm above the ramp for experiments 3-8 and 90 mm to 120 mm for for experiments 1 and 2. These data were sampled from 60 seconds of data within the body of the experiments. The error bars are the standard deviation of the measured TKE at each bin.

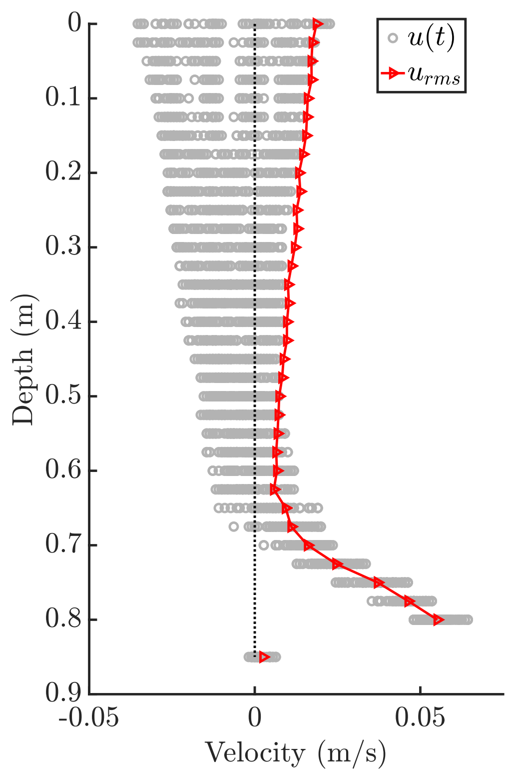

Figure 3.10: Time series for 10 seconds of downstream velocity (u) measured by an Acoustic Doppler Profiler at a sampling frequency of 8 Hz. This profile is taken from experiment 7, a high flow experiment, 8 m from the rear of the flume. The root-mean-square is in the bright line with triangle markers. Note the decay of the wave signal from the surface down to the body of the underlying current.

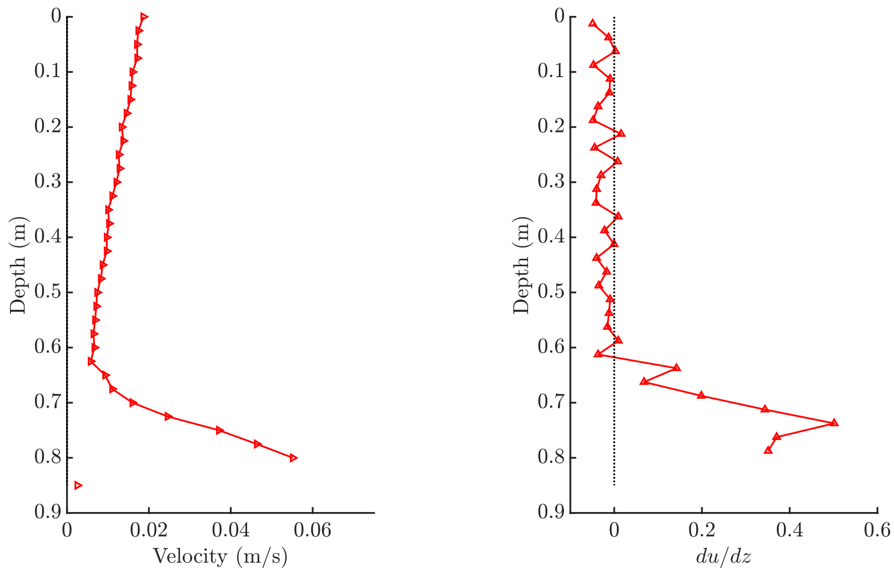

Figure 3.11: On the left, the root-mean-square profile of the data referred to in Figure 3.10. This profile is taken from experiment 7, a high flow experiment, 8 m from the rear of the flume. On the right, the vertical gradient of the profile on the left.

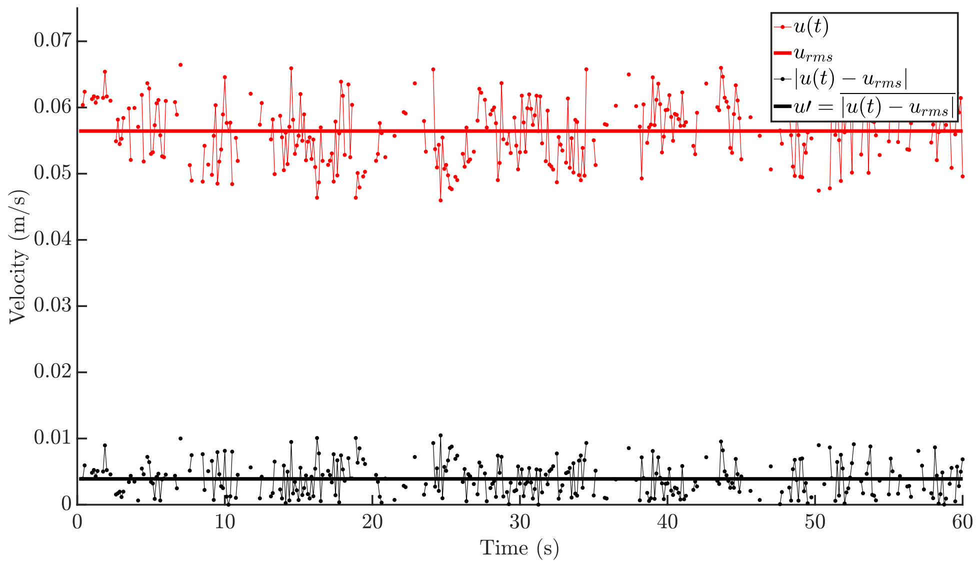

Figure 3.12: Extracting the deviatoric velocity component from Acoustic Doppler Profiler (ADP) velocity data in the bin 5 cm above the ramp, in the bin with the highest velocities. The solid red line is the time series of the velocity at a single depth bin within the body of the combined flow. The dashed red line is the root-mean-square of the time series. The black solid line is the absolute value of the time series and the root-mean-square, and the dashed black line is the mean. This value is used to characterize the average instantaneous fluctuating behavior at a given location. This data was taken at the maximum velocity core of the current, 5 cm above the ramp, at the downslope-most ADP profile for flow 7, a high flow experiment, referred to in Figure 3.10 and Figure 3.11.

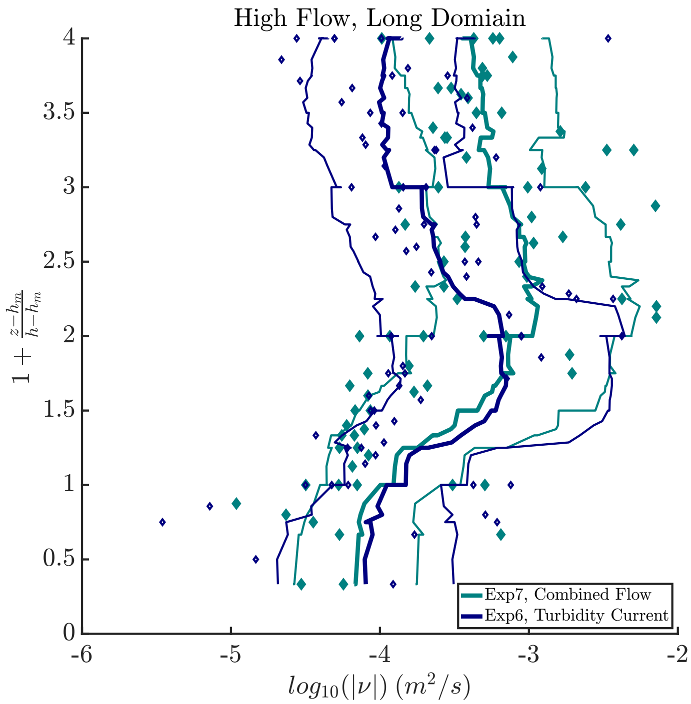

Figure 3.13: The eddy viscosity of combined flows (Experiment 7) and their coupled current without waves (Experiment 6), plotted in relative elevation space, from the bed to four times the current thickness. These experiments are low flow in a short domain (Table 3.1). The y-axis values of 0 correspond to the bed, unity is the height of the center of the current, 2 is the top of the current, and the intervals above are multiples of the current thickness. These data are taken across the ramp during each flow. The bold line is a one-sided moving average of the data, and the fine lines are the moving standard deviation.

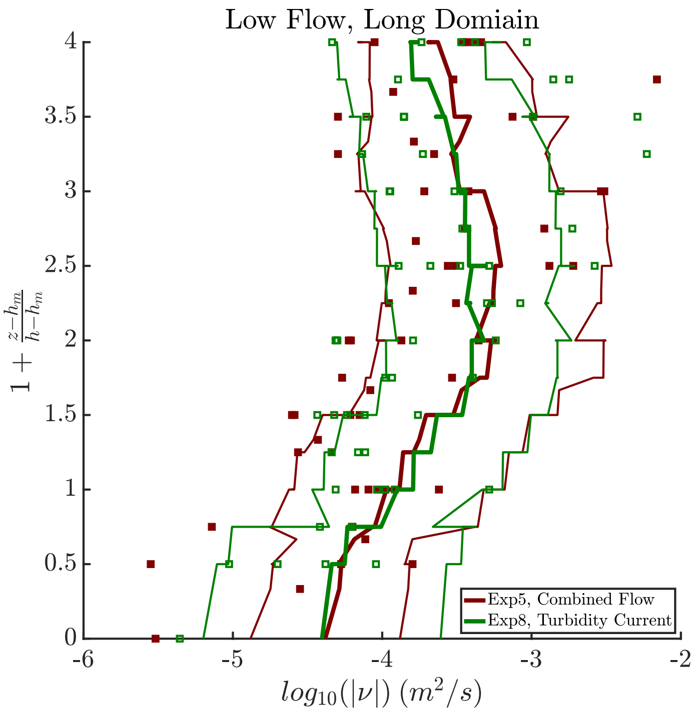

Figure 3.14: The eddy viscosity of combined flows (Experiment 5) and their coupled current without waves (Experiment 8), plotted in relative elevation space, from the bed to four times the current thickness. These experiments are low flow in a short domain (Table 3.1). The y-axis values of 0 correspond to the bed, unity is the height of the center of the current, 2 is the top of the current, and the intervals above are multiples of the current thickness. These data are taken across the ramp during each flow. The bold line is a one-sided moving average of the data, and the fine lines are the moving standard deviation.

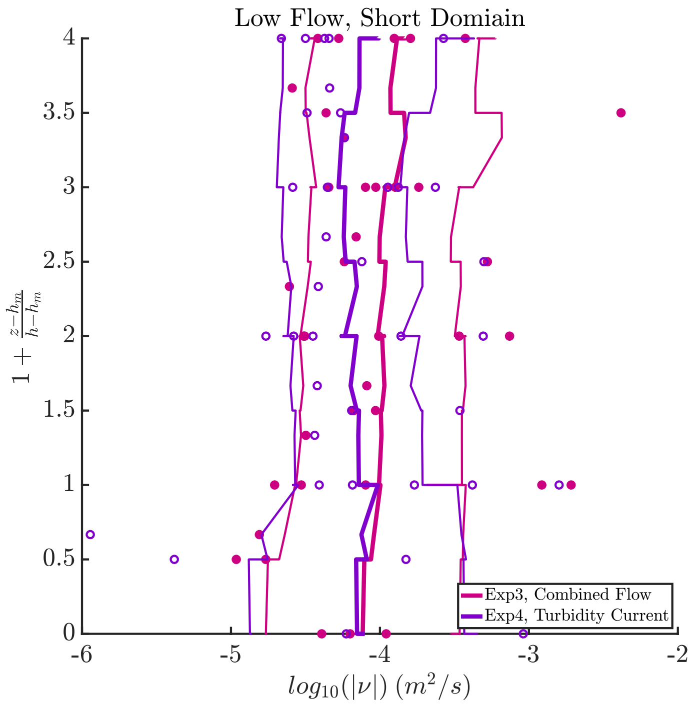

Figure 3.15: The eddy viscosity of combined flows (Experiment 3) and their coupled current without waves (Experiment 4), plotted in relative elevation space, from the bed to four times the current thickness. These experiments are low flow in a short domain (Table 3.1). The y-axis values of 0 correspond to the bed, unity is the height of the center of the current, 2 is the top of the current, and the intervals above are multiples of the current thickness. These data are taken across the ramp during each flow. The bold line is a one-sided moving average of the data, and the fine lines are the moving standard deviation.

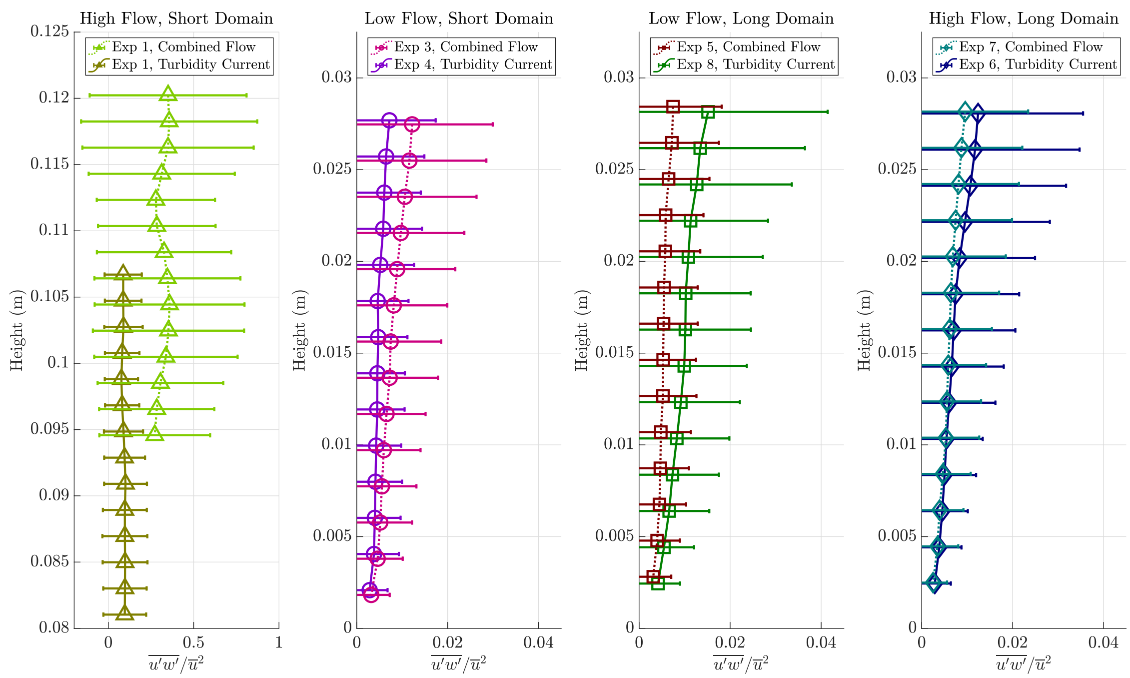

Figure 3.16: Reynolds shear stress measurements ($\tau_R = \overline{u'w'}$) as a function of depth. In all experiments except experiments 1 and 2, which measure far from the bed, combined flows have greater turbulent stress than their corresponding flow without waves. These data were taken at the downstream end of the flume (8.31 m from the rear of the flume) from 0 mm to 30 mm above the ramp for experiments 3-8 and 90 mm to 120 mm for for experiments 1 and 2. These data were sampled from 60 seconds of data within the body of the experiments. The error bars are the standard deviation of the measured value of $u'w'$ at each bin.

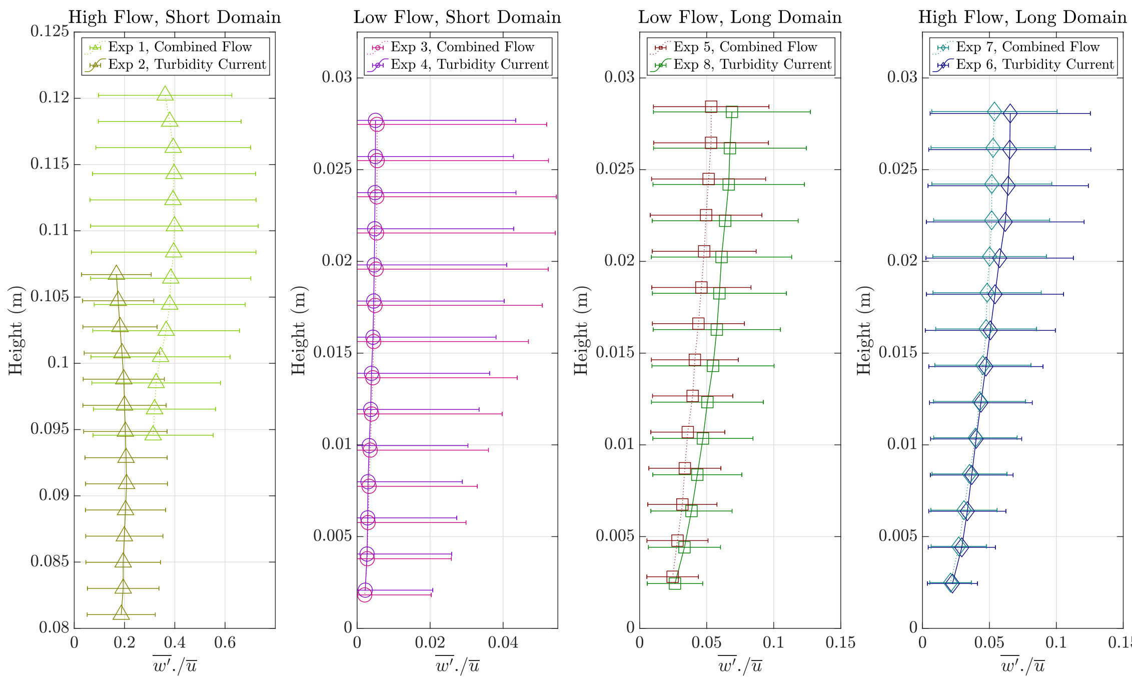

Figure 3.17: The vertical turbulent component, w', normalized by the downstream mean velocity, $\overline{u}$, measured by the downslope Profiling Velocimeter. In all cases, combined flows have reduced vertical turbulent components. These data were taken at the downstream end of the flume ($8.31\,m$ from the rear of the flume) from $0\,mm$ to $30\,mm$ above the ramp for experiments 3-8 and $90\,mm$ to $120\,mm$ for for experiments 1 and 2. These data were sampled from 60 seconds of data within the body of the experiments. The error bars are the standard deviation of the measured value of w' at each bin.

Chapter 4

Detrital Zircon Transport Lag in Bedload and Incipient Suspended Transport

4.1 Introduction

Zircons are a common accessory mineral in siliciclastic sediment sources. This mineral contains up to one part in a hundred of radioactive U and Th, which decays to daughter products with known half-lives, forming the basis of the U-Th-Pb geochronometer. Because zircons are so durable chemically and physically, they are considered and excellent and representative "fingerprints" of their source rock (Vermeesch, 2012).

Studies that use detrital zircon geochronology assume that the statistical metrics measuring dissimilarity between samples can be used to determine distinct sedimentary sources (Saylor and Sundell, 2016; Vermeesch, 2018; Ibañez-Mejia et al., 2018). However, provenance studies consistently show that detrital zircon U-Pb ages are also correlated to grain size (Sircombe et al., 2001; Garzanti et al., 2009; Lawrence et al., 2011; Ibañez-Mejia et al., 2018). The size distribution of sediment changes along the length of a single bedform, but this principle of bedform transport-filtering has yet to be applied to detrital zircons sampling regime. Moreover, previous studies consistently suggest that the dynamics of sediment transport are strongly dependent on grain size, shape, and density (Stokes, 1851; Udden, 1914; Shields, 1936; Rouse, 1937; Dietrich, 1982; Viparelli et al., 2015). Recently, Ibañez-Mejia et al. (2018) found that simple significance testing of samples is insufficient to determine whether a sample is truly from multiple sources, or a single mode transport-lagged in time. This represents a profound opportunity to integrate traditional sediment transport relationships into detrital zircon studies, including the transportability of grains into age estimates and investigating the transport filtering effect an individual bedform has on dense grains.

Conceptually, the modes of transport that grains can travel along a river with bedforms can be observed in Figure 4.1. Grains can be lagged behind an overall dune on the stoss slope and subsequently buried. Grains can be transported along the back side of the stoss, to the lee, and be avalanched down. These can be buried over by the migrating dune. These grains can also be recycled into the body of the dune. Grains can be transported to the crestline and avalanche down the lee face, or hop to the next dune. It is important to note that once a grain is buried, it is no longer being transported at the individual-event timescale. Its transport is on geologic time. Grains also can suspend into the fluid column. In each one of these scenarios, grains of different densities, sizes, and shapes will exhibit different behaviors at different rates, and when these propensities are integrated over large time and space scales, they can introduce spatial heterogeneity in a sedimentary system. If the mode of transport and the transport histories for bulk sediment and tracer grains are different, then the tracer is not representative of bulk sediment. One problem that may arise is overestimating ages or misidentifying an age provenance because the dense tracers' transport time is substantial enough to skew a distribution.

4.1.1 Objectives

In this chapter, I report the results of experiments that investigate the dynamics of transport of dense grains (e.g., magnetite) within a less-dense bulk sediment load of quartz sand. Our general question is: to what degree do dense tracers reflect the transport histories of bulk quartz sediment? To test this, I turn to the measured concentration of particles preserved within the body of the dune. To what degree does a single bedform filter and winnow dense sediments, and under which transport conditions is this effect large? Are the grains found in the deposits characteristic of differing modes of sediment transport? Our experiments represent a best-case scenario, with no sediment burial, and particle transport rate as a function only of the exerted shear by the flow.

This paper aims to establish an understanding of the mechanics of sediment transport in a detrital zircon context. Using a set of experiments, I show the lagging process of dense grains associated with movement of a single unidirectional bedform, and develop a simple set of sampling principles to choose dense tracer grains that represent bulk sediment in various transport settings.

4.2 Methods

I conducted experiments in the Experimental Sedimentology Lab at the University of Texas at Austin, using an 11 m long recirculating flume (Figure 4.2). The flume is 0.6 m wide and 1.2 m deep. Using a flow diffuser at the upstream end, I am able to generate a logarithmic flow-velocity profile, measured by a Nortek Aquadopp Acoustic Doppler Profiler. One meter from the flow diffuser, a 2 m long by 50 mm thick bed of sand was smoothed to cover the base of the flume (Figure 4.3, first time step). Our sand mixture included 90 kg of medium quartz sand, $D_{50} = 281\ \mu m$, $\rho_{qtz} = 2616 kg/m^3$ and $1 kg$ of magnetic sediment, $D_{50} = 330 \mu m$, $\rho_{mag} = 4990 kg/m^3$.

I conducted experiments under four different transport conditions (Table 4.1): both sands moving as bedload at a low rate (experiment 5); both sands moving as bedload at a higher rate (experiments 4 and 6); quartz in incipient suspension while magnetic sediment is in bedload (experiments 3 and 7); and quartz in incipient suspension while magnetic sediment is in bedload but at a higher rate (experiments 2 and 8). Because of the non-linear effect of flow velocity on the mode of transport and topography, I found that I was able to incipiently suspend some grains of each kind, and were able to also transport both as only bedload, which is expanded upon in the Results and Discussion sections. The mean vertically-averaged centerline flow velocities associated with the four transport conditions were 0.155 m/s (experiment 5), 0.159 m/s (experiments 4 and 6), 0.161 m/s (experiments 3 and 7), and 0.188 m/s (experiments 2 and 8). Despite a modest range in mean flow velocities between the experiments, I was able to generate a wide variety of transport conditions because our experiments operated at thresholds for different types of transport. Our experiments were paused periodically throughout their duration to take an elevation scan of the deposits. The experiments' total durations were 420 min, 242 min, 140 min and 140 min. Overhead photopans were also taken of the deposits.

The experiments were run until the bedform translated one full wavelength past its initial deposition location (Figure 4.3). Given that sediment transport rates are highly variable, with some grains moving quickly, and others moving slowly, as long as every grain moved at least once in our domain I was certain that our data accurately reflects the overall transport behavior of sediment under the flow conditions I imposed.

After the transport condition were satisfied, hand samples were taken. After draining the tank, samples were taken at 0.25 m intervals along the centerline of the deposit. A 0.5 l plastic scooping cup was inserted into the bed from the top of the deposit to the base of the flume to include the entire sediment column in the sample. These samples were dried in an oven before magnetic sediment was separated out of the samples with a magnet. Each dry sample was spread thinly over a pan, and a strong ceramic magnet wrapped in plastic was repeatedly drawn through the sediment, extracting the magnetic grains. This method was able to extract at a minimum 1 g of magnetic material out of 1 kg of sediment. The magnetic and non-magnetic samples were then weighed to determine their mass concentrations.

A Retch Camsizer, Model P2, optical grain size analyzer was used to determine the grain size. The quartz sediment was placed in a vibrating chute, which poured sediment in a plane parallel to a high speed camera that photographed the sediment. The instrument determines the grain size distribution of the sediment.

Because the magnetic sediment is magnetically cohesive, its grain size could not be analyzed on its own. The magnetic force between the grains causes them to clump, and skew the distribution to appear coarser than it actually is. To remedy this, each magnetic sand sample was mixed with glass spheres with a known, narrow size distribution ($D_{50} = 175\,\mu m$, $\sigma = 0.15$, Very Well sorted). This disaggregated the magnetic sand. The size distribution was determined by subtracting the known glass spheres' distribution from the combined distribution, and fitting a normal distribution to the data.

4.3 Results

4.3.1 Time Lapse Elevation Maps and Sediment Flux

Using time lapse elevation scans taken periodically during the duration of each experiment, I am able to quantify the bedload flux associated with the translation of the single bedform in each experiment. As an example, the time lapse surface of experiment 2 is presented in Figure 4.3. From these scans, I use the area translated between the mean bedform profiles.

$$q_b = (1 - \lambda)A/t, \tag{4.1}$$

where λ is the bedform porosity (assumed to be 0.3), A is the translated area, calculated with the brinkline and lee-toe locations from scan to scan, and t is the time between scans.

In all the experiments the flux measured from the translation of the bedform decreases as the bedform translates. I note that the flux used in our shear stress calculations in the Discussion section use the average flux from the last 60 minutes of each experiments' duration.

4.3.2 Magnetic Concentration Profiles

The concentration profile of magnetic sand particles is a function of the relative vigor of bulk transport (Figure 4.4). To make the experiments comparable, the concentrations are normalized against the initial concentration of magnetic sand to quartz, 1:90 by mass.

The lowest flow condition, experiment 5, has a strong lag behavior at the upstream end of the stoss slope, almost double the initial concentration. Within the body of the dune up to the lee face, the concentration is approximately 30% greater than the initial concentration. At the lee face, the concentration decreases below the initial concentration to 40%.

The low flow conditions, experiments 4 and 6, have a strong lag at the upstream of the bedform, 2.3 times greater than the initial, decreasing to equal to the initial concentration within the bedform in experiment 4. In experiment 6, the concentration decreases within the body of the bedform to as low as 70% of the original. In both experiments the concentration of magnetic particles decays to 30% and 40% of the original concentration.

The medium flow conditions, experiments 3 and 7, also display a lag at the upstream end of the bedform. Within the bedform the concentration is approximately equivalent to the original in experiment 3, or decreases to near the initial concentration in experiment 7. Both have a strong depletion beyond the lee face to less than 50% the initial concentration.

The high flow conditions, experiments 2 and 8, have different lag behaviors than the other experiments. Experiment 2 and 8 have qualitatively different curves from one another: experiment 2 has no lagged tail, while experiment 8 does. Both however, have steady concentrations within the body of the dune itself. Experiment 2 has a 25% depletion, while the experiment 8 is only 10% depleted. Both have an enrichment of magnetic material at the dune crest of 28% and 53%. In experiment 8, there is depletion at and beyond the lee face to 30% the original. Experiment 2 has approximately the original concentration at the lee face, and no data beyond.

4.3.3 Grain Size and Sorting

4.3.3.1 Quartz Sand

In all the experiments, with the exception of experiment 8, the quartz grain size within the bedform approximates the original distribution (Figure 4.5). Beyond the lee face, the median grain size decreases.

The grain sorting, σ, is calculated using the Folk and Ward method,

$$\sigma = \frac{\Phi_{84} - \Phi_{16}}{4} + \frac{\Phi_{95} - \Phi_5}{6.6}, \tag{4.2}$$

where Φ_n is the nth percentile of the grain size distribution in the Wentworth Scale ($\Phi = log_2 \frac{D}{D_0}$). In all experiments, quartz grain sorting remained constant over the domain at the threshold of "Well Sorted" to "Very Well Sorted" ($\sigma = 0.35$, Figure 4.7).

4.3.3.2 Magnetic Sand

The median magnetic sediment grain size (input , $D_{50mag} = 330\mu m$), had a similar grain size trend as quartz in the downstream direction (Figure 4.6). The median grain size remains constant within the body of the bedform and decreases beyond the lee face. Experiments 2 and 8 are the exceptions: experiment 2 coarsens at the crestline, and experiment 8 stays constant in the measured domain.

The sorting behavior of magnetic sand is different than the quartz sand (Figure 4.7). While sorting remained constant for all the quartz samples in all the experiments, the magnetic sand had variable results. The lowest flow condition, experiment 5, is less well sorted at the crestline and lee face than in the rear of the dune, and subsequently becomes better sorted beyond the dune at the threshold of "Well Sorted" to "Very Well Sorted."

The low flow conditions, experiments 4 and 6, improve their sorting along the length of the bedform, crossing the threshold to "Very Well Sorted." Beyond the lee face, experiment 4 becomes better sorted. Experiment 6 maintains its sorting and becomes less sorted beyond one full dune wavelength from the lee face.

The medium flow conditions, experiments 3 and 7, maintain their sorting within the bedform. Beyond the lee face, the two experiments' behavior deviate slightly. Both have better sorting approximately $0.75\,m$ from the lee face, but the sorting in experiment 7 returns to that measured within the bedform, while the sorting in experiment 3 becomes better with distance from the lee face.

In high flow conditions, experiment 2, sorting is less well-sorted than that measured in the other experiments, though it similarly improves along the length of the bedform starting at "Moderately Sorted" at the rear, becoming "Well Sorted." The sorting in experiment 8 is consistently "Well Sorted" in the bedform and beyond the lee face.

4.4 Discussion

From experiment to experiment, I observe different transport outcomes for the two sediment types. In low flow experiments, the dense tracer particles mostly lag at the rear of the dune. In the high flow experiments, the tracers are enriched at the crestline. To determine the transport conditions at the grain scale, I present an inverse model to calculate the stress required to transport the bedform. I then determine the suspension propensity for our two types of grains, and their nominal saltation hop velocity. I also discuss these grain-scale parameters in the context of a bedform-scale analysis of the types of lag I observed.

4.4.1 Inverse Modeling Skin Friction

Beginning with the known sediment transport conditions measured in the flume, I determine the stress required to transport the sediment measured in the experiments (Equation 4.1, Table 4.1). Rather than estimating parameters from fluid flow, I can directly determine the bed stress that transported the sediment in the experiments.

The component of the bed shear stress, τ_{sf}, affecting sediment transport is referred to as "skin friction stress." Skin friction stress is only a small component of the total boundary shear stress, τ_b, exerted by the flow, $\tau_b = \tau_{sf} + \tau_{fd}$ (Nelson and Smith, 1989; Mohrig and Smith, 1996; Nittrouer et al., 2011). The form drag stress, τ_{fd}, is the component of the total stress associated with the roughness elements on the channel bed like grains, dunes, and topography. I calculate the skin friction stress values from the known q_b values referred to in the Results section (Equation 4.1).

Bedload transport is related to the difference between the skin friction stress and the critical shear stress required to move the median sediment of the bed. These terms are non-dimensionalized by the following:

$$\tau^* = \frac{\tau}{(\rho_s - \rho_f) g D_{50}}, \tag{4.3}$$

where ρ_s is sediment density, ρ_f is fluid density, g is gravitational acceleration, and D_{50} is the median grain size.

The bedload transport rate of sediment with a single mode can be described by the relationship relating the exceedance of stress relative to the critical stress required for sediment motion, τ_c^*:

$$q_b^* = \gamma(\tau_{sf}^* - \tau_c^*)^{1.5} \tag{4.4}$$

where q_b^* relates to the bedload sediment per unit width of flow q_b as

$$q_b^* = \frac{q_b}{\sqrt{(RgD_{50}^3}} \tag{4.5}$$

R is the specific gravity of the sediment $((\rho_s - \rho_f)/\rho_f)$. The exceedance threshold is modified by a parameter γ, first proposed by Meyer-Peter and Muller in 1948, and has been frequently modified depending on the composition of sediment. Wiberg and Rubin (1989), and Mohrig and Smith (1996), allow γ to vary as a function of the non-dimensional skin friction stress,

$$\gamma = 1.6 ln(\tau_{sf}^*) + 9.8 \tag{4.6}$$

Combining Equation 4.6, Equation 4.5, and Equation 4.3, and inputting them into Equation 4.4, I can determine the required skin friction stress for the sediment transport I observe in each experiment. I determine the shear velocity at the bed with the following:

$$u_{sf} = \sqrt{\frac{\tau^*_{sf}}{\rho_f}} \tag{4.7}$$

The values for each experiment are reported in Table 4.1; as transport increases, so does stress.

4.4.2 Suspended Sediment Potential and Escape from the Bedform

A grain is considered to be in suspended load when it is advected in the fluid column. Bedload is defined as grains transporting by rolling, sliding or saltating along the bed. The ratio between the settling velocity and the shear velocity (w_s/u_{sf}), characterizes the mode of transport of a particular grain size (Rouse, 1937). The settling velocity equation II used was Ferguson and Church (2004):

$$w_s = \frac{(RgD_n^2)}{C_1\nu + (0.75C_2RgD_n^3)^{0.5}} \tag{4.8}$$

where C_1 and C_2 are parameterized values of 20 and 1.1 for natural grains using the nominal diameter (Ferguson and Church (2004), fitting Dietrich (1982) natural grains).

With our inverse model-derived shear velocities (Equation 7, Table 4.1), and the calculated settling velocity from each grain (Equation 4.8), I determine grain settling velocity to shear velocity ratio for each grain size measured in our domain (Figure 4.8). I can combine this with the known frequencies of those grain sizes and determine a cumulative frequency distribution for the grain settling velocity to shear velocity ratio (Figure 4.9).

Using the threshold of $w_s/u_{sf} < 3$, where grains are incipiently suspended as the weak threshold for grains to incipiently suspend, and $w_s/u_{sf} < 1$, as the threshold for full suspension ((Bagnold, 1966; Nishimura and Hunt, 2000; Niño et al., 2003)), I compare these calculated values to our experimental results . The primary distinction between the magnetic tracer sediment and the bulk quartz sediment transport regimes predicted by the model is the propensity for full suspension. In every experiment, the threshold for full suspension ($w_s/u_{sf} < 1$) is barely met for magnetic sediment (less than 3 percent). However, the degree of incipient suspension ($w_s/u_{sf} < 3$) varies the smallest 11 percent of grain sizes in lowest flow, to 45 to 90 percent of the load in the medium and high flow cases. As discussed in the Methods section, despite a modest range in mean flow velocities between experiments, I was able to generate a range of sediment transport conditions because our inputs were near threshold for different modes of transport.

Bulk quartz sediment is almost entirely in the mode of either incipient or full suspension, though the high flow and medium flow have almost 30 to 50 percent of grain sizes with a propensity for full suspension, and the lowest flow only has 10 percent.

In all experiments, excluding the high flow experiments 2 and 8, the magnetic sediment lags at the rear of the dune (Figure 4.4). In these cases, sediment retention in the bedform is relatively high, over 95%, with the exception of experiment 7 (Table 4.1). In contrast, the high flow experiments have a greater degree of sediment suspended away from the bedform, approximately 10 percent. This suspension of sediment indicates a strong degree of vigorous transport.

To summarize, the sediment suspension model indicates that bulk quartz gains transport vigorously as bedload, and a non-negligible fraction have the propensity for full suspension in the experiments with high flow, which is borne out by the measured lost volume in the experimental bedforms (Figure 4.9, Table 4.1). Magnetic grains are predicted to transport as bedload, or with a fraction as incipiently suspended in the high flow experiments. The concentration profile of the magnetic sediment in the high flow cases indicate strong transport by the magnetic sediment, keeping pace with the bulk sediment, though that does not account for the volume of quartz lost to suspended load. The dense particles keep pace with bedload in high transport conditions. Some magnetic particles are able to be transported beyond the bedform as suspended load, but as the depleted concentration profiles beyond the crestline indicate, they are a small fraction of the magnetic sediment ensemble.

4.4.3 Calculating Grain Hop Velocity

In addition to the propensity for sediment suspension, another grain-scale characteristic that informs transport similarity is the grain hop velocity, u_b. The grain hop velocity is resolvable using our flux-calculated skin friction. First, I determine the transport stage parameter of each flow, after Rijn (1984):

$$T^* = \frac{(u^{*'})^2 - (u^*_{cr})^2}{(u^*_{cr})^2}. \tag{4.9}$$

In this relationship, u^*_{cr} is the critical shear velocity for the median grain size of interest, calculated using the Brownlie (1981) analytical formulation of the Shields

Curve (Shields, 1936). The bed shear velocity, $u^{*'}$, related to grains is defined by Rijn as the following:

$$u^{*'} = \overline{u}g^{0.5}/C' \tag{4.10}$$

where $\overline{u}$ is the mean flow velocity, C' is the Chezy coefficient related to grains using the Vanoni-Brooks sidewall correction (Vanoni and Brooks, 1957). The coefficient is calculated by:

$$C' = 18log_{10}\frac{12R_b}{(3D_{90})} \tag{4.11}$$

with R_b, is the hydraulic radius related to the bed according to the sidewall correction of Vanoni and Brooks. Using the calculated transport stage (Equation 4.9), Van Rijn developed a model framework for the nominal grain hop velocity for grains.

$$\frac{u_b}{RgD_{50}^{0.5}} = 1.5T^{0.6} \tag{4.12}$$

The calculated hop velocities and ratios between them are reported in Table 4.2. The ratio between quartz and magnetic sand hop velocities is 1.72, 1.62, 1.59, and 1.29 for the lowest flow, the low flow, the medium flow, and the high flow conditions, respectively. As the transport stage for each type of sediment increases in flows of increasing velocity, their hop velocities become increasingly similar (Figure 4.10). Sediment with the same transport stage will have the same non-dimensionalized grain hop velocity. In the high flow cases (experiments 2 and 8), which correspond to some suspended sediment transport for bulk sediment, and vigorous bedload transport for the magnetic sediment, the two types of grains saltate at velocities within 30 percent of one another. This behavior's effect on the transport is confirmed by the concentration profiles of magnetic sediment (Figure 4.6). Magnetic sediment is constant within the body of the bedform and is concentrated at the crestline, indicating transport commensurate with the rate of the bulk quartz bedform. Conversely, in the other experiments, hop velocity ratio is higher, and while both materials move as bedload, there is a strong lag at the rear of the dune.

4.4.4 Where does one pick grains that transport at the same rate?

This relationship between the similarity grain-scale parameters like transport mode and hop velocity, and the observed concentration profile in the dune can be used diagnostically. Starting with the concentration profile of dense tracers in a bedform, one can deduce under what circumstances, and at which locations in the bedform, bulk sediment and dense tracers transport at similar rates.

The two types of lag behavior observed in the reported experiments are (1) lag behind the bedform in low to medium flow, and (2) lag at the crestline in high flow (Figure 4.6). In the first set of cases, low and medium flow, bulk sediment moves as bedload, and magnetic sediment also moves as bedload, but not as vigorously (experiments 5, 4 and 6, Figure 4.9). In these experiments, the two sediments' transport are decoupled. Despite a nominally similar transport mode, the calculated hop velocities of the median grains are substantially different from one another, and this is reflected in the lag behavior I observe, with high concentrations at the rear of the dune. In our experimental domain the lagging grains are exposed on a non-erodible bed, and are collected at the stoss of the dune. In a natural setting, those grains would be trapped at the lee face of the bedform behind it, and captured by burial (Figure 4.1). Once that happens, those buried grains become part of the geologic record, and are not transported at the timescale of a single event.

If I compare the grain size distributions of the magnetic sediment that is lagged versus the escaped particles, I observe distinct fining over a single bedform (Figure 4.11). The grain sizes of the materials that are lagged are similar to the initial grain size distribution. However, the ejected materials are finer than the lagged materials. The transport and the bedform itself act as a filter for dense grains. The lagged grains represent the initial distribution of magnetic sediment, but do not transport at the rate of bulk quartz sediment. The coarser grains lag, and would be buried in a natural setting. The finer grains that escape the bedform can represent the suspended fraction, but are not representative of the initial distribution, or of bulk transport.

The dense grains that may transport at the same rate as their quartz neighbors are those traveling in suspended load, though they represent a small fraction of total transport. As I observed, the suspended load fraction of dense grains are finer and better sorted than those grains in the bedform (Figure 4.7). There is the possibility that those grains with similar settling velocities have comparable travel times, but they are not representative of bulk transport. Moreover, the percent of the overall grain size population of the dense grains which are governed by their settling velocity, ($w_s/u_{sf} < 1$), is smaller than the finest 1 percent in every experiment (Figure 4.9).

Only a very small fraction of the dense tracer grain population reflect the suspended load transport in every experiment. To effectively sample them, they must be picked at the base of the lee face of a dune near the surface, and are only comparable to grains in a similar location, and not within the body of the bedform. This ensures that they are not compared with exhumed grains that were previously captured and buried. It bears mentioning that these lower flow cases are bedload-dominated, and can hardly be said to be represented by the finest sediment in suspension.

In the case of high flow transport, where sampling reveals enrichment of dense, coarse sediment at the crestline, those dense grains do travel at the same rate as bulk sediment. This is provided that there is not too much loss to suspended load, though the presence of bedforms is a helpful guide in that regard. A fully suspended load dominated regime would transition to upper plane bed (Paola et al., 1989). In this case, if one assumes that most sediment in source to sink scenarios moves as bedload, even under vigorous transport conditions, then the dense tracer minerals at the crestline transport at the same rate as their neighboring quartz gains.

One can also examine the dense tracer grains that are transported in suspended load. While grains in suspended load are comparable in terms of their calculated settling velocities, only a small percent of the overall distribution is representative of this behavior, as in the low flow cases. In the case where bulk sediment transport is primarily in bedload, the grains at the base of the lee face are the comparable suspended load fraction.

4.4.5 Estimated Zircon Lag Behavior in the Lower Mississippi River

Based on work completed by Nittrouer et al. (2011), these experimental results can be compared with a large, natural system: The Lower Mississippi in high flow, April, 2008. In addition to measuring the sediment flux in bedload and suspended load, Nittrouer et al. applied a similar inverse model for sediment transport, calculating the skin friction stress required to translate a set of bedforms during a flood.

The total sand discharge in the Lower Mississippi in April, 2008 was reported to be an average of 11,988 tons per hour at river kilometers 35-47. In their survey, over half of the sediment mass was measured as suspended load, with a suspended load median grain size commensurate with the finest 10 percent of bedload grain sizes.

The model developed by Rijn is inappropriate to use in this context because of the extremely high transport stage. The reported skin friction shear stresses calculated for the flow, ($\overline{\tau_{sf}} = 8.19\ Pa$) results in a transport stage a far greater magnitude than the required stress to mobilize the median grain size ($\overline{T^{*}} = 39$ for grains $D_{50} = 200\ \mu m$). Because of the overwhelming degree of transport in the Mississippi, even though the ratio of transport stages is in the model domain ($T^{*}_{mag}/T^{*}_{qtz} = 0.55$), the most salient variable that affects the hop velocity is the component of specific density. As a result, grains with greater density or size are disproportionately predicted to have high hop velocities and overpredicts the velocity of dense grains.

The settling velocity to shear velocity ratio is an informative metric for this setting (Figure 4.8). Both materials are overwhelmingly in the full suspended load regime, which is borne out by the data collected by Nittrouer et al. They found the median bed sediment in the uppermost tenth of the fluid column. In fact, because of the high degree of transport in the system, the finest in the Mississippi are captured by bedforms, and the suspended load in transport and dense tracer minerals found there can be characterized by those dense grains that are found in similar locations with similar settling velocities. In the bedload, the transport stages of dense grains of equivalent size found in the same location would be more similar, sampling tracer minerals found at the crestline as representative of the bedload transport.

In such a high energy system, which is able to transport extremely large amounts of bulk sediment in suspension, an effective sampling practice for finding representative grains can take two forms. To accurately characterize the suspended fraction, which is significant in this case, tracer minerals should be sampled from the lee face with similar settling velocities as the suspended load particles of interest. To accurately sample the bedload materials, dense tracers should be samples from the crestlines, where they keep pace with bulk sediment in bedload.

4.5 Conclusions

In this study, I investigated the transport lag of dense particles relative to ambient sediment, analogous to detrital zircons transported in fluvial bedload. The question I aimed to answer was: given detrital zircon and quartz grain, side by side in a deposit, did they take the same amount of time to transport to that location? I found that quartz grains transport faster than detrital zircons, and the degree in difference is controlled by the transport mode (i.e., bedload and suspended load) of sediment transport that both types of grains experience. Most importantly I show that bedforms have a strong filtering effect on dense grain transport, lagging grains at the stoss, and preferentially transporting fine material beyond the dune, leaving coarser materials behind.

From our results I can determine several factors controlling the relative grain velocity of trace dense particles in bedload. First, dense materials are not evenly distributed within a single bedform, with heterogeneous grain size distributions along the profile of a single dune. Moreover, the concentration profile relative to the mean can indicate what the mode of transport for each type of grain was. Dense particle lag at the stoss-slope indicates both transporting as bedload flux, lag around the crestline indicates bulk sediment incipiently suspending. Uniform concentration throughout the bedform would indicate synchronous transport.

Second, as transport stage increases for both materials, their ratio approaches unity. As a consequence, the modeled hopping velocity of the grains converge; the bulk sediment and dense tracers move more similarly in vigorous bedload transport.

Third, I provide a framework for sampling dense tracers that reflect certain parts of bulk sediment transport. In low flow conditions, evidenced by lag in the stoss of a dune, the bedload transport of the two materials is decoupled. The suspended load can be reflected in the finer component of the dense tracers collected at the bottom of the dune lee face. In high flow conditions, with vigorous bedload transport, but minimal loss to suspended load, the bedload transport can be accurately represented with the dense tracers collected at the crestline of the dune. Suspended load can be characterized by the fine tracers at the lee face.

When compared to an extremely high-energy, large-scale system, like the Lower Mississippi, I recommend that in-channel samples be taken at the dune crestline for bedload modeling, and at the base of the lee face for suspended load.

Lastly, I want to stress the winnowing effect that bedforms have on dense particle transport. The grains that escape the bedform are not representative of the initial size distribution, and they are not reflective of those grains that are lagged, either. Both are a function of the transport conditions they experience, and those conditions are heterogeneous on the dune scale.

Our experiments represent a best-case scenario for a fluvial system transporting grains, where all materials are being transported with no burial. In fluvial systems at the threshold for transport and in locations where dense sediment is buried or fractioned from the system in other ways like point bars or floodplains, dense grains have the potential for even greater lag and decoupling from bulk sediment.

Table 4.1: Experiments organized by input mean flow velocity.

Experiment	Mean Flow Velocity, $\overline{u}$, (m/s)	Bedload Flux, q_b, (m^2/s)	Shear Velocity, u^*_{sf}, (m/s)	Volume Fraction Retained in Bedform's Final Hour
2	0.1877	20.55e-06	0.0351	0.89
8	0.1877	14.09e-06	0.0315	0.81
3	0.1610	17.43e-06	0.0335	0.96
7	0.1610	9.17e-06	0.0279	0.85
4	0.1593	7.49e-06	0.0263	0.97
6	0.1593	6.80e-06	0.0256	0.98
5	0.1548	3.15e-06	0.0207	0.95

Table 4.2: Model outputs of each experiment.

Experiment	Shear Velocity, u^*_{sf}, (m/s)	Quartz Sand Transport Stage, Van Rijn (1984a), T^*, ( )	Magnetic Sand Transport Stage, Van Rijn (1984a), T^*, ( )	Median Quartz Sand Particle Hop Velocity, u_b, (m/s)	Median Magnetic Sand, Particle Hop Velocity, u_b, (m/s)
2	0.0122	3.68	1.01	0.221	0.172
8	0.0113	3.70	1.02	0.222	0.172
3	0.0124	2.43	0.47	0.172	0.109
7	0.0106	2.45	0.48	0.173	0.110
4	0.0097	2.39	0.45	0.171	0.106
6	0.0099	2.38	0.45	0.170	0.106
5	0.0081	2.23	0.39	0.16 4	0.096

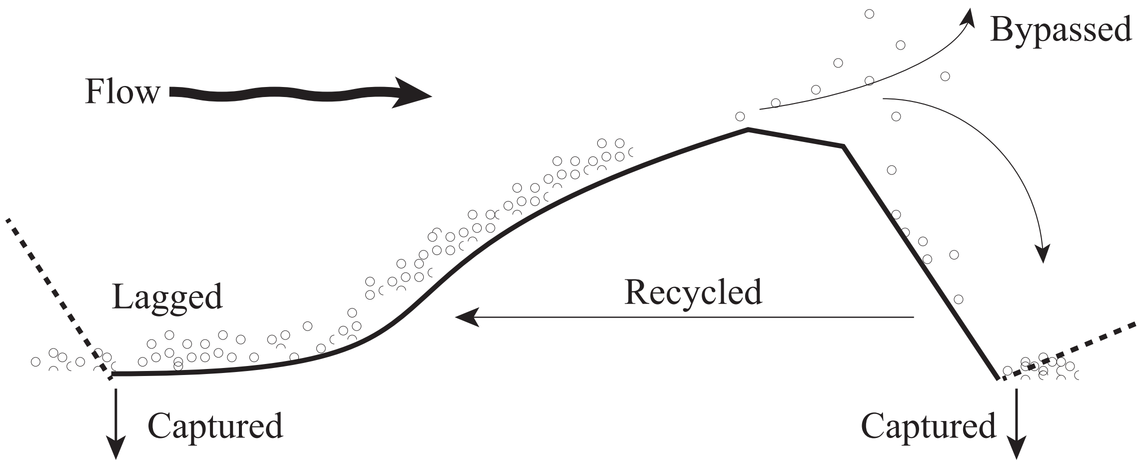

Figure 4.1: A conceptual diagram of the different processes of sediment transport that make up a bedform. Grains can be lagged behind the bar and buried, they can be transported along the stoss slope and recycled into the body of the bedform. Grains can be transported to the crestline and avalanche down the lee face, to be transported into the next bedform, they can also be buried. Grains at the crestline can also be ejected into the fluid column as suspended load, or they can be recaptured into a dune trough, re-transported, or buried.

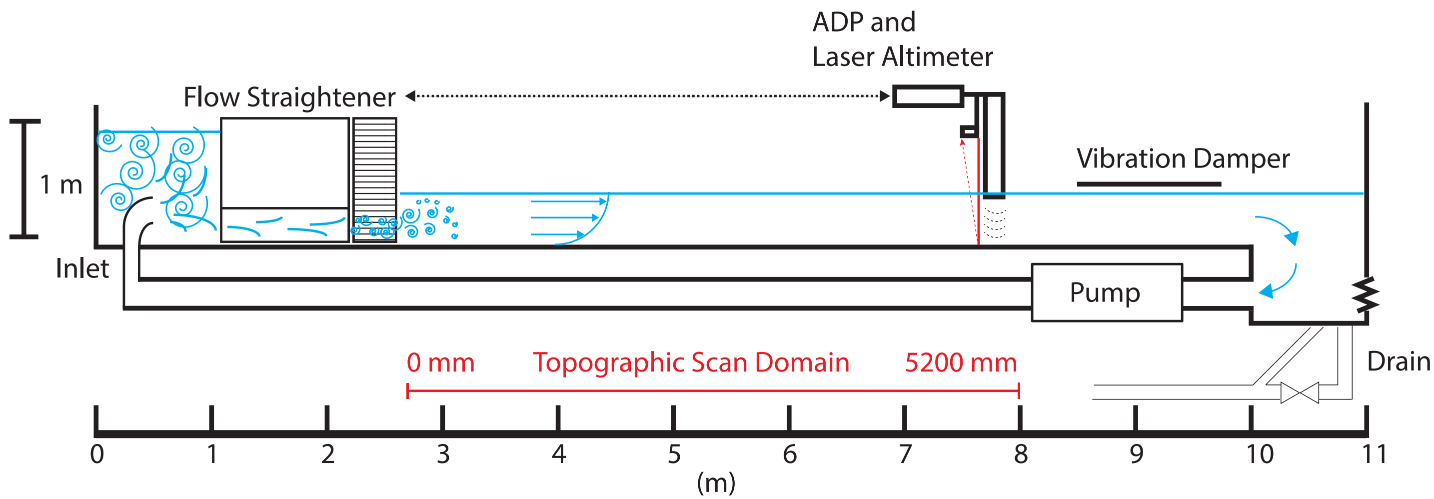

Figure 4.2: A vertically exaggerated schematic of the experimental setup: The Long Flume in the Experimental Sedimentology Lab at the University of Texas at Austin. The flume measures 11 m long, 1.2 m deep, and 0.6 m wide.

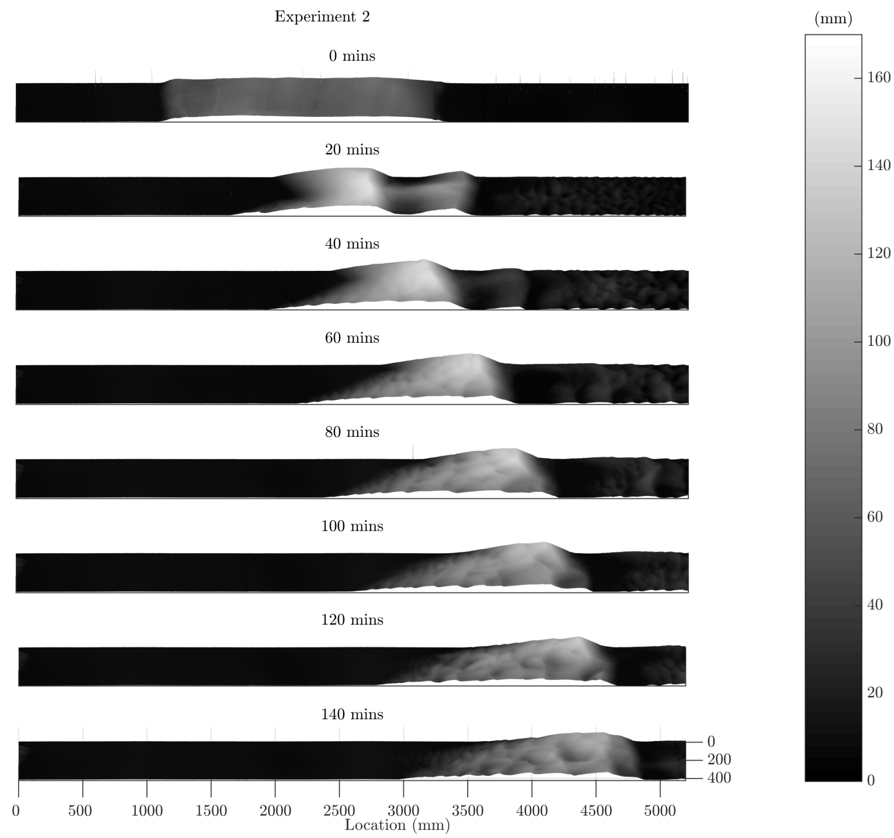

Figure 4.3: Time lapse elevation maps taken with a Keyence laser altimeter. The sediment is initially deposited as a plane bed 1-3 m from the inlet and allowed to transport until all the sediment has moved past its initial deposition site, ensuring all sediment has been transported.

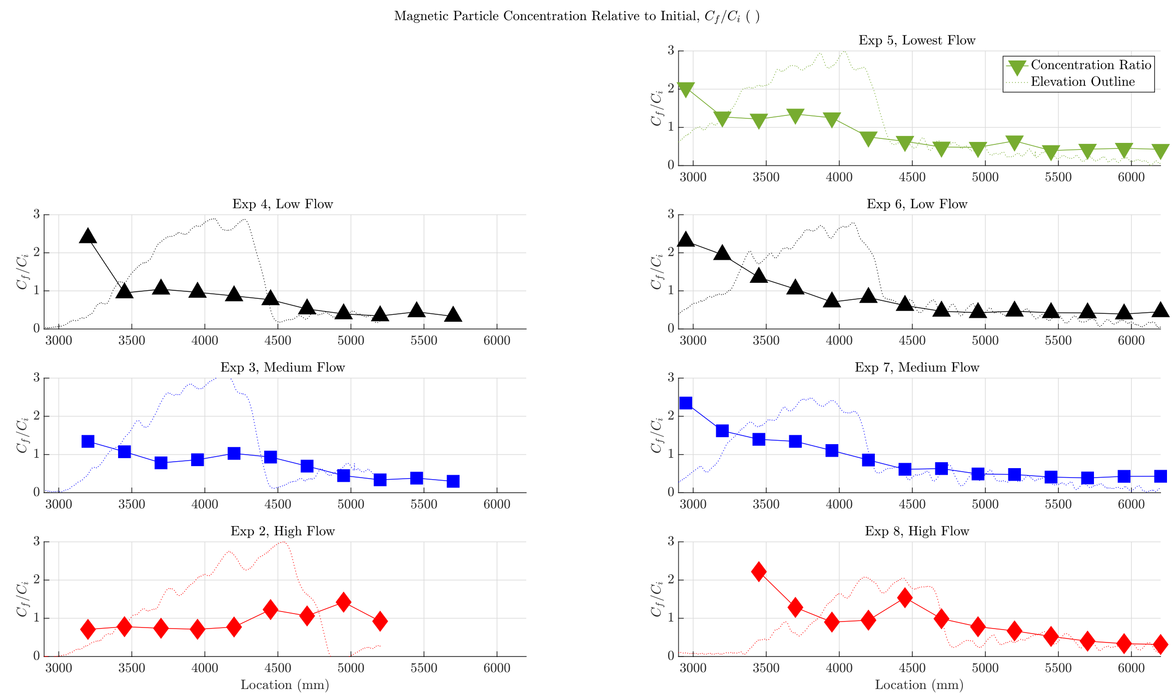

Figure 4.4: The mass concentration relative to the initial (1:90 by mass) of magnetic sediment along the length of the deposit. The deposit outlines are in the dotted lines. All runs have a lag at the rear end of the dune, except experiment 2. Experiments 2 and 8, the high flow runs, have a lag around the crestline, due to dune deflation from quartz suspended sediment transport, which leaves the dense materials behind.

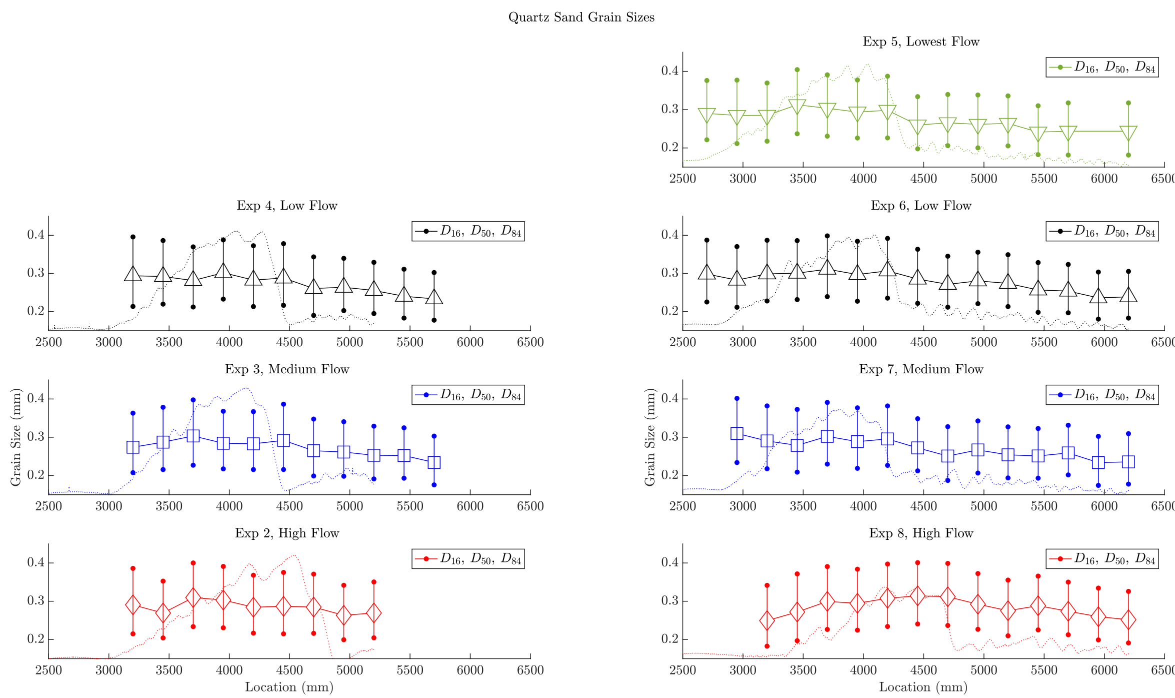

Figure 4.5: Quartz grain size data taken after each experiment. The markers represent the D_{16}, D_{50}, and D_{84}. The outline of the bedform is the dotted line.

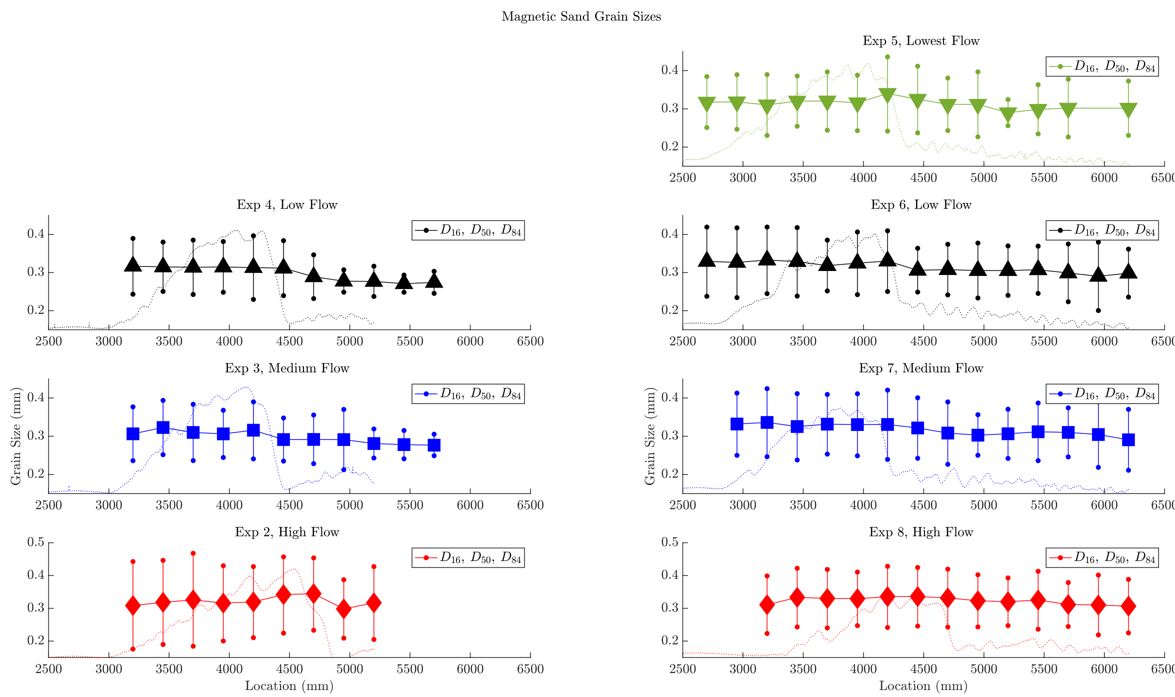

Figure 4.6: Magnetic sediment grain size data taken after each experiment. The markers represent the D_{16}, D_{50}, and D_{84}. The outline of the bedform is the dotted line.

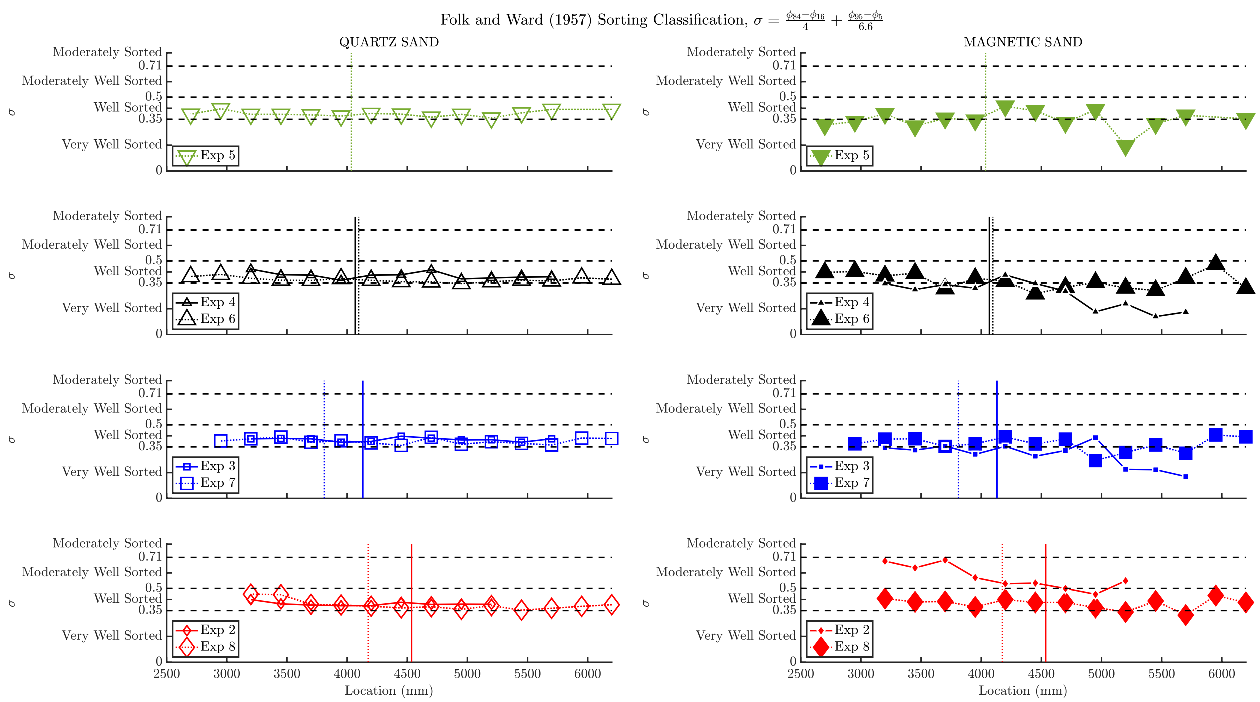

Figure 4.7: Folk and Ward (1957) sorting classification of sediment samples (Figure 4.5 and Figure 4.6), derived using Equation 4.2.

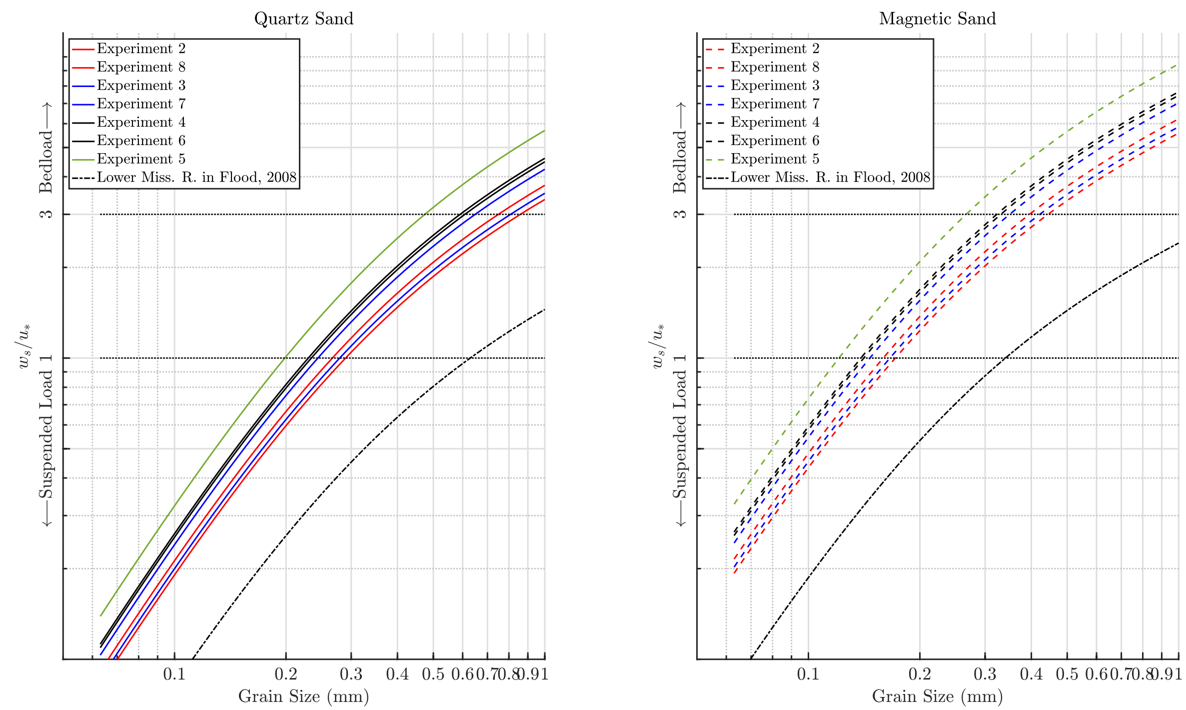

Figure 4.8: Based on the initial grains size range, the ratio of the grain settling velocity and skin friction shear velocity for each experiment is computed for both quartz and magnetic sediments. The values for the same sediment range for the Lower Mississippi River in flood are also plotted (based on the results from Nittrouer et al. (2011)).

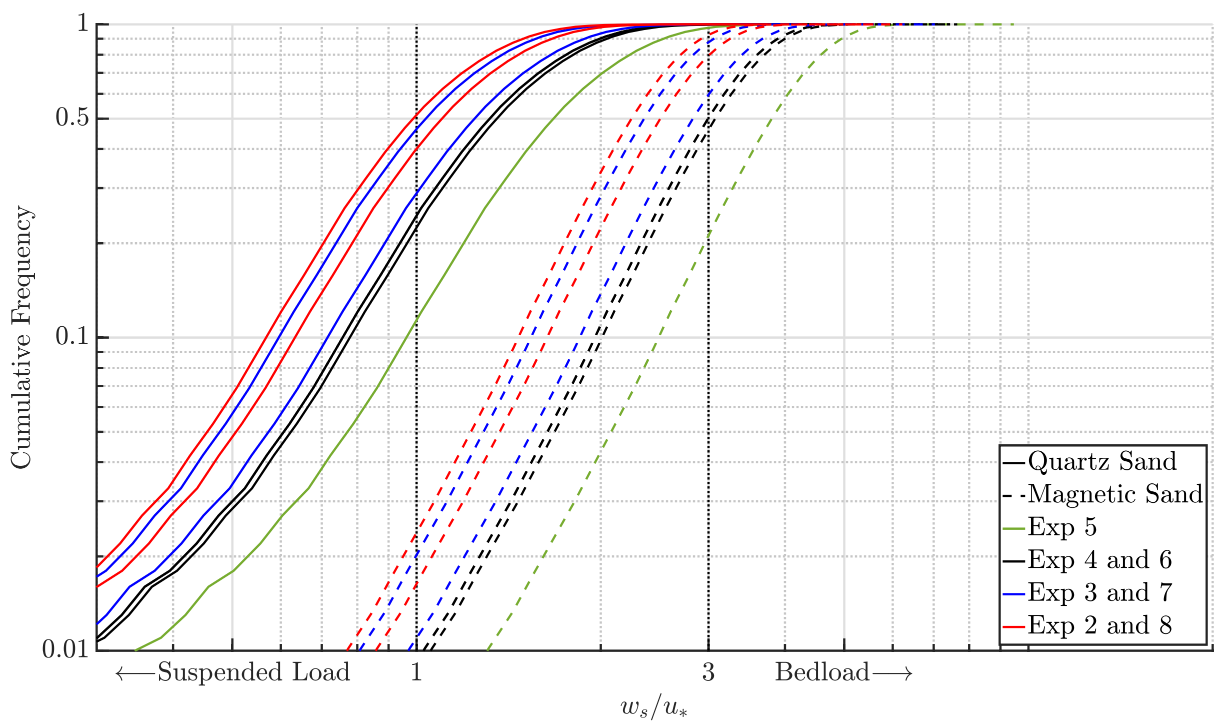

Figure 4.9: The Rouse Numbers of each experiment, determined by using the shear required to transport the sediment wave. The solid lines are the quartz sediment, and the dashed lines are the magnetic sediment

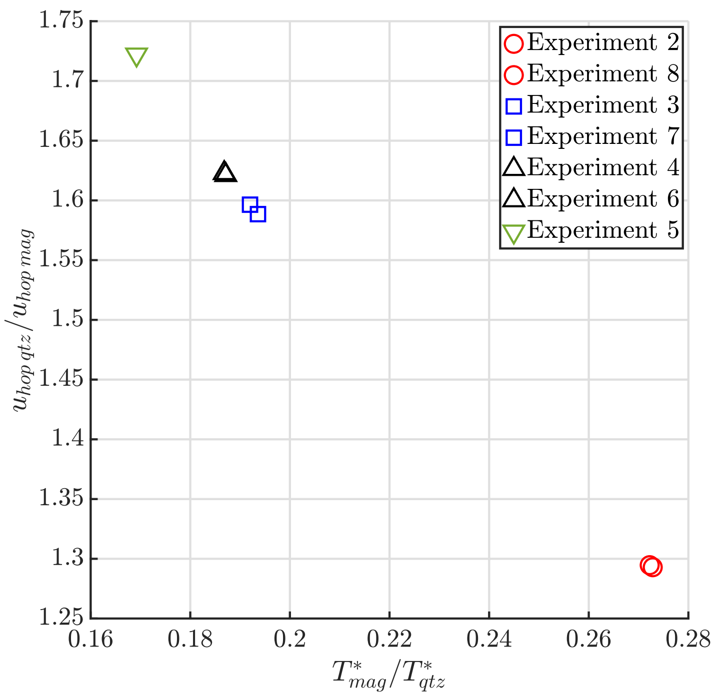

Figure 4.10: The ratio of experimental transport stage ratios of magnetic sediment over quartz sediment plotted against the computed hop velocity ratio, after Rijn (1984). As the vigor of transport increases, and the ratio between the transport stages of quart and magnetic sand converge, the ratio of the two sediments' hop velocities approaches unity. The materials transport in bedload at the same speed.

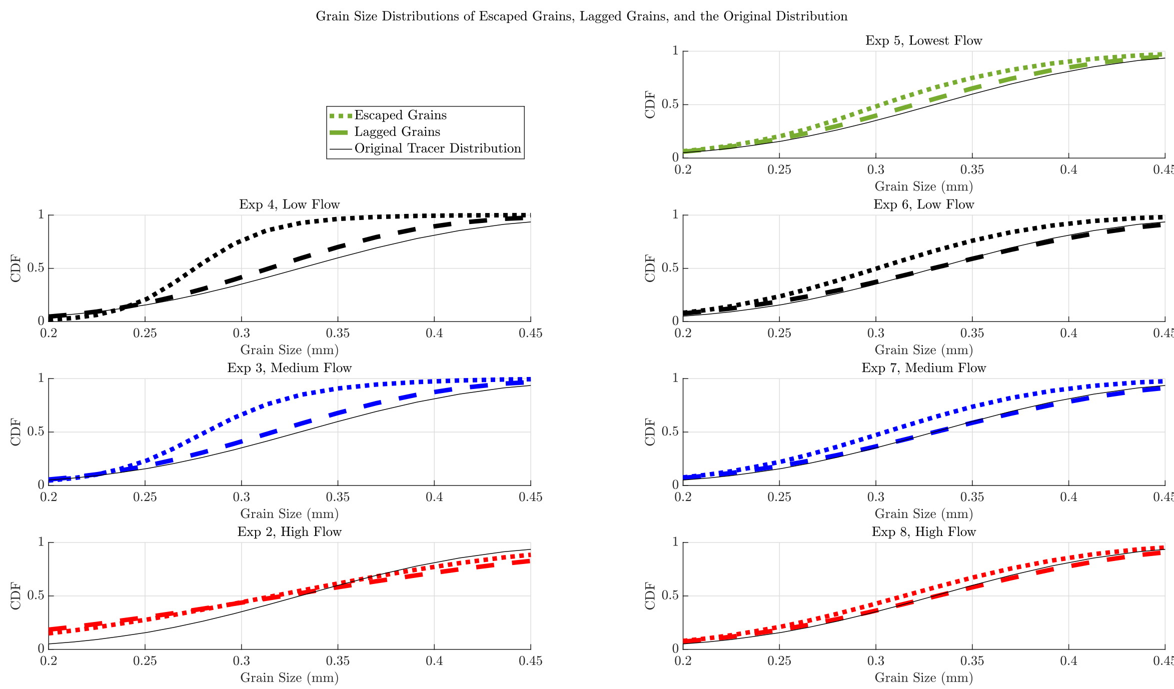

Figure 4.11: The cumulative density functions of the input magnetic sediment grain sizes (sold lines), and the distributions of the lagged (dashed lines) and escaped (dotted lines) grain size distributions. The grains that escape are all finer than the original distribution and the lagged grains.

Chapter 5

Conclusions and Future Directions

The results of this dissertation demonstrate how fragile assumptions of steadiness and homogeneity are when tested. All of the experiments in this dissertation show how profoundly sediment transport and landscape evolution are affected by weakly unsteady and marginally heterogeneous systems are strongly a function of their respective non-uniformity. Not only do I point to the effects, but I thoroughly investigate the processes involved, and provide some metrics and tools for characterizing the degree of change as a function of the forcing, or reducing it from a sampling technique.

The study on the effect of flooding cycles intermingled with periods of normal flow in Chapter 2 provides a useful conceptual metric, Intermittency, for interpreting delta island arrangement and morphology. I found in my experiments that the more frequently a system is in flood relative to normal flow, the shorter the length to bifurcations. This relationship is important because the flooding history of a deltaic system can be inferred by its constituent islands. This is a particularly significant contribution in cases where flow data is unavailable but with good exposure, such as planetary systems, or in outcrop.

Chapter 3 furthers research in the field of combined flow sediment transport, experimentally studying the effects of wave fields on sediment gravity currents. How wave fields imprint in the sedimentary record is a long-standing debate in the field of sediment transport, and the presence of an oscillating field and its deposits are used diagnostically for identifying the paleo-envrioment in coastal stratigraphy. I show that the presence of a wave signal is not sufficient to positively categorize a coastal environment as above "wave-base." Sediment gravity currents can transport a wave signal from the near shore to deeper waters.

Diving further into the findings, I found that not only are wave signals within combined flows, and by extension, their deposits, misplaced, but that waves fundamentally alter the dynamics of mixing within those combined flows. The wave field can disrupt the exchange of fluid between a current and ambient fluid, inducing a periodic component of mixing, reducing vertical diffusion of momentum, which has a host of sediment transport effects, notably increasing downslope transport for bulk sediment. Note that, the wave field I imposed was relatively weak. Future work will investigate the effect of stronger waves on features like grain size and the symmetry of ripples.

The final project in Chapter 4 investigates the types of lag that dense grains have in bulk sediment transport. A widely-used technique in geochronological research is the use of various dense, durable tracer particles with predictable radionuclide decay. These particles are used as representative tracers of bulk sediment transport, despite little research into the different transport rates of these particles.

My experiments indicate that there are several modes of dense particle lag in these systems. In bedload transport conditions, the dense tracer transport is entirely decoupled from bulk sediment transport. In suspended load conditions, the tracers at the crestline can be used as a representative of bulk transport, and grains that escape by suspension may also be comparable. However, the fact that I was able to generate a strong filtering effect over the length scale of a single bedform indicates a profound opportunity to investigate the effect over a larger scale with multiple bedforms, and in unsteady flow conditions where the bedform is moving from one equilibrium to another.

Bibliography

Airy, G. On tides and waves. *Encylopaedia Metropolitana*.

Altinakar, M., W. Graf, and E. Hopfinger (1996). Flow structure in turbidity currents. *Journal of Hydraulic Research 34*(5), 713–718.

Baas, J., W. McCaffrey, P. Haughton, and C. Choux (2005). Coupling between suspended sediment distribution and turbulence structure in a laboratory turbidity current. *Journal of Geophysical Research: Oceans 110*(C11).

Bagnold, R. (1966). *An approach to the sediment transport problem from general physics*. US government printing office.

Bates, C. (1953). Rational theory of delta formation. *AAPG Bulletin 37*(9), 2119–2162.

Blum, M. and H. Roberts (2009). Drowning of the Mississippi Delta due to insufficient sediment supply and global sea-level rise. *Nature Geoscience 2*(7), 488–491.

Blum, M. and H. Roberts (2012). The Mississippi delta region: past, present, and future. *Annual Review of Earth and Planetary Sciences 40*, 655–683.

Brownlie, W. (1981). Prediction of flow depth and sediment discharge in open channels.

CPRA (2017). Louisiana's Comprehensive Master Plan for a Sustainable Coast. *Baton Rouge: Coastal Protection and Restoration Authority*.

CPRA (2019). Integrated Ecosystem Restoration & Hurricane Protection in Coastal Louisiana Fiscal Year 2019 Annual Plan. *Baton Rouge: Coastal Protection and Restoration Authority*.

Dietrich, W. (1982). Settling velocity of natural particles. *Water resources research 18*(6), 1615–1626.

Dingler, J. and D. Inman (1976). Wave-formed ripples in nearshore sands. *Coastal Engineering Proceedings 1*(15).

Edmonds, D. and R. Slingerland (2007). Mechanics of river mouth bar formation: Implications for the morphodynamics of delta distributary networks. *Journal of Geophysical Research: Earth Surface 112*(F2).

Ferguson, R. and M. Church (2004). A simple universal equation for grain settling velocity. *Journal of sedimentary Research 74*(6), 933–937.

Folk, R. and W. Ward (1957). Brazos river bar [texas]; a study in the significance of grain size parameters. *Journal of Sedimentary Research 27*(1), 3–26.

Foster, D. and D. Stone (1963). Ocean disposal of ash: The university of new south wales. *Water Research Laboratory, Report 65*, 130.

Garzanti, E., S. Andò, and G. Vezzoli (2009). Grain-size dependence of sediment composition and environmental bias in provenance studies. *Earth and Planetary Science Letters 277*(3-4), 422–432.

Hiatt, M. and P. Passalacqua (2015). Hydrological connectivity in river deltas: The first-order importance of channel-island exchange. *Water Resources Research 51*(4), 2264–2282.

Holthuijsen, L. (2007). *Waves in oceanic and coastal waters.* Cambridge university press.

Ibañez-Mejia, M., A. Pullen, M. Pepper, F. Urbani, G. Ghoshal, and J. Ibañez-Mejia (2018). Use and abuse of detrital zircon u-pb geochronology?a case from the río orinoco delta, eastern venezuela. *Geology 46*(11), 1019–1022.

Inman, D. (1957). Wave-generated ripples in nearshore sands. Technical report, Scripps Institution Of Oceanography, La Jolla Ca.

Jaramillo, S., A. Sheremet, M. Allison, A. Reed, and K. Holland (2009). Wave-mud interactions over the muddy atchafalaya subaqueous clinoform, louisiana, united states: Wave-supported sediment transport. *Journal of Geophysical Research: Oceans 114*(C4).

Kämpf, J. and P. Myrow (2014). High-density mud suspensions and cross-shelf transport: on the mechanism of gelling ignition. *Journal of Sedimentary Research 84*(3), 215–223.

Kämpf, J. and P. Myrow (2018). Wave-created mud suspensions: a theoretical study. *Journal of Marine Science and Engineering 6*(2), 29.

Kim, W., D. Mohrig, R. Twilley, C. Paola, and G. Parker (2009). Is it feasible to build new land in the Mississippi River Delta. *Eos 90*(42), 373–374.

Kneller, B. and C. Buckee (2000). The structure and fluid mechanics of turbidity currents: a review of some recent studies and their geological implications. *Sedimentology 47*, 62–94.

Lamb, M., B. McElroy, B. Kopriva, J. Shaw, and D. Mohrig (2010). Linking river-flood dynamics to hyperpycnal-plume deposits: Experiments, theory, and geological implications. *Bulletin 122*(9-10), 1389–1400.

Lamb, M., P. Myrow, C. Lukens, K. Houck, and J. Strauss (2008). Deposits from wave-influenced turbidity currents: Pennsylvanian minturn formation, colorado, usa. *Journal of Sedimentary Research 78*(7), 480–498.

Lawrence, R., R. Cox, R. Mapes, and D. Coleman (2011). Hydrodynamic fractionation of zircon age populations. *Bulletin 123*(1-2), 295–305.

Lesser, G., J. Roelvink, J. Van Kester, and G. Stelling (2004). Development and validation of a three-dimensional morphological model. *Coastal engineering 51*(8), 883–915.

Liapidevskii, V., D. Dutykh, and M. Gisclon (2018). On the modelling of shallow turbidity flows. *Advances in water resources 113*, 310–327.

Ma, Y., C. Friedrichs, C. Harris, and L. Wright (2010). Deposition by seasonal wave- and current-supported sediment gravity flows interacting with spatially varying bathymetry: Waiapu shelf, new zealand. *Marine Geology 275*(1-4), 199–211.

Massey, F. (1951). The kolmogorov-smirnov test for goodness of fit. *Journal of the American statistical Association 46*(253), 68–78.

Mohrig, D. and J. Smith (1996). Predicting the migration rates of subaqueous dunes. *Water Resources Research 32*(10), 3207–3217.

Mulder, T., J. Syvitski, S. Migeon, J. Faugeres, and B. Savoye (2003). Marine hyperpycnal flows: initiation, behavior and related deposits. a review. *Marine and Petroleum Geology 20*(6-8), 861–882.

Myrow, P., W. Fischer, and J. Goodge (2002). Wave-modified turbidites: combined-flow shoreline and shelf deposits, cambrian, antarctica. *Journal of Sedimentary research 72*(5), 641–656.

Myrow, P. and J. B. Southard (1991). Combined-flow model for vertical stratification sequences in shallow marine storm-deposited beds. *Journal of Sedimentary Research 61*(2), 202–210.

Myrow, P. and J. B. Southard (1996). Tempestite deposition. *Journal of Sedimentary Research 66*(5), 875–887.

Nelson, J. M. and J. Smith (1989). Mechanics of flow over ripples and dunes. *Journal of Geophysical Research: Oceans 94*(C6), 8146–8162.

Nienhuis, J., J. Perron, J. C. Kao, and P. Myrow (2014). Wavelength selection and symmetry breaking in orbital wave ripples. *Journal of Geophysical Research: Earth Surface 119*(10), 2239–2257.

Niño, Y., F. Lopez, and M. Garcia (2003). Threshold for particle entrainment into suspension. *Sedimentology 50*(2), 247–263.

Nishimura, K. and J. Hunt (2000). Saltation and incipient suspension above a flat particle bed below a turbulent boundary layer. *Journal of Fluid Mechanics 417*, 77–102.

Nittrouer, J., D. Mohrig, and M. Allison (2011). Punctuated sand transport in the lowermost mississippi river. *Journal of Geophysical Research: Earth Surface 116*(F4).

Norton, B. (2005). *Sustainability: A philosophy of adaptive ecosystem management.* University of Chicago Press.

Paola, C., P. Heller, and C. Angevine (1992). The large-scale dynamics of grain-size variation in alluvial basins, 1: Theory. *Basin Research 4*(2), 73–90.

Paola, C., S. Wiele, and M. Reinhart (1989). Upper-regime parallel lamination as the result of turbulent sediment transport and low-amplitude bed forms. *Sedimentology 36*(1), 47–59.

Parker, G., C. Paola, K. Whipple, and D. Mohrig (1998). Alluvial fans formed by channelized fluvial and sheet flow. I: Theory. *Journal of Hydraulic Engineering 124*(10), 985–995.

Parsons, J., C. Friedrichs, P. Traykovski, D. Mohrig, J. Imran, J. Syvitski, G. Parker, P. Puig, J. Buttles, M. García, et al. (2007). The mechanics of marine sediment gravity flows. *Continental Margin Sedimentation: From Sediment Transport to Sequence Stratigraphy, C. Nittrouer, J. Austin, M. Field, J. Syvitski, and P. Wiberg, eds., Blackwell, Oxford, UK*, 275–333.

Passalacqua, P. (2017). The Delta Connectome: A network-based framework for studying connectivity in river deltas. *Geomorphology 277*, 50–62.

Pedocchi, F. and M. Garcia (2009). Ripple morphology under oscillatory flow: 1. prediction. *Journal of Geophysical Research: Oceans 114*(C12).

Perillo, M., J. Best, and M. Garcia (2014). A new phase diagram for combined-flow bedforms. *Journal of Sedimentary Research 84*(4), 301–313.

Perillo, M., J. Best, M. Yokokawa, T. Sekiguchi, T. Takagawa, and M. Garcia (2014). A unified model for bedform development and equilibrium under unidirectional, oscillatory and combined-flows. *Sedimentology 61*(7), 2063–2085.

Perron, T., P. Myrow, K. Huppert, A. Koss, and A. Wickert (2018). Ancient record of changing flows from wave ripple defects. *Geology 46*(10), 875–878.

Piliouras, A., W. Kim, and B. Carlson (2017). Balancing aggradation and progradation on a vegetated delta: the importance of fluctuating discharge in depositional systems. *Journal of Geophysical Research: Earth Surface 122*(10), 1882–1900.

Rijn, L. (1984). Sediment Transport, Part I: Bed Load Transport. *Journal of Hydraulic Engineering 110*(10), 1431–1456.

Rouse, H. (1937). Modern conceptions of the mechanics of fluid turbulence. *Trans ASCE 102*, 463–505.

Rowland, J., M. T. Stacey, and W. E. Dietrich (2009). Turbulent characteristics of a shallow wall-bounded plane jet: experimental implications for river mouth hydrodynamics. *Journal of Fluid Mechanics 627*, 423–449.

Saylor, J. and K. Sundell (2016). Quantifying comparison of large detrital geochronology data sets. *Geosphere 12*(1), 203–220.

Sequeiros, O. (2012). Estimating turbidity current conditions from channel morphology: A froude number approach. *Journal of Geophysical Research: Oceans 117*(C4).

Shaw, J. B. and D. Mohrig (2014). The importance of erosion in distributary channel network growth, Wax Lake Delta, Louisiana, USA. *Geology 42*(1), 31–34.

Shields, A. (1936). Application of similarity principles and turbulence research to bed-load movement.

Simpson, J. (1997). *Gravity currents: In the environment and the laboratory* (2nd ed.). Cambridge University Press.

Sircombe, K., W. Bleeker, and R. Stern (2001). Detrital zircon geochronology and grain-size analysis of a 2800 ma mesoarchean proto-cratonic cover succession, slave province, canada. *Earth and Planetary Science Letters 189*(3-4), 207–220.

Smith, E., M. Daniller-Varghese, P. Myrow, and D. Mohrig (2019). Exparimental inverstigations of combined flow sediment transport. *Journal of Sedimentary Research 89*, 1–7.

Starr, V. (1968). Physics of negative viscosity phenomena. *Earth and Planetary Science Series 256*.

Stokes, G. (1851). *On the effect of the internal friction of fluids on the motion of pendulums*, Volume 9. Pitt Press Cambridge.

Tal, M. and C. Paola (2007). Dynamic single-thread channels maintained by the interaction of flow and vegetation. *Geology 35*(4), 347–350.

Traykovski, P., P. Wiberg, and W. Geyer (2007). Observations and modeling of wave-supported sediment gravity flows on the po prodelta and comparison to prior observations from the eel shelf. *Continental Shelf Research 27*(3-4), 375–399.

Udden, J. (1914). Mechanical composition of clastic sediments. *Bulletin of the Geological Society of America 25*(1), 655–744.

Vanoni, V. and N. Brooks (1957). Laboratory Studies of the Roughness and Suspended Load of Alluvial Streams. *California Institute of Technology 112*(1), 130.

Vermeesch, P. (2012). On the visualisation of detrital age distributions. *Chemical Geology 312-313*, 190–194.

Vermeesch, P. (2018). Dissimilarity measures in detrital geochronology. *Earth-Science Reviews 178*, 310–321.

Viparelli, E., L. Solari, and K. Hill (2015). Downstream lightening and upward heavying: Experiments with sediments differing in density. *Sedimentology 62*(5), 1384–1407.

Walsh, J. and C. Nittrouer (2009). Understanding fine-grained river-sediment dispersal on continental margins. *Marine Geology 263*(1-4), 34–45.

White, B. and K. Helfrich (2008). Gravity currents and internal waves in a stratified fluid. *Journal of Fluid Mechanics 616*, 327–356.

Wiberg, P. and C. Harris (1994). Ripple geometry in wave-dominated environments. *Journal of Geophysical Research: Oceans 99*(C1), 775–789.

Wiberg, P. L. and D. M. Rubin (1989). Bed roughness produced by saltating sediment. *Journal of Geophysical Research 94*(C4), 5011–5016.

Wright, L. (1977). Sediment transport and deposition at river mouths: a synthesis. *Geological Society of America Bulletin 88*(6), 857–868.

Wright, L., J. Boon, S. Kim, and J. List (1991). Modes of cross-shore sediment transport on the shoreface of the middle atlantic bight. *Marine Geology 96*(1-2), 19–51.

Wright, L. and C. Friedrichs (2006). Gravity-driven sediment transport on continental shelves: a status report. *Continental Shelf Research 26*(17-18), 2092–2107.

Wright, L., C. Friedrichs, S. Kim, and M. Scully (2001). Effects of ambient currents and waves on gravity-driven sediment transport on continental shelves. *Marine Geology 175*(1-4), 25–45.

Zavala, C., J. Ponce, M. Arcuri, D. Drittanti, H. Freije, and M. Asensio (2006). Ancient lacustrine hyperpycnites: a depositional model from a case study in the rayoso formation (cretaceous) of west-central argentina. *Journal of Sedimentary Research 76*(1), 41–59.

Vita

Max Sasha Daniller-Varghese was born in Austin, Texas the summer of 1992, the son of Mae M. Daniller and Prof. Philip L. Varghese. He received the Bachelor of Science degree in Earth Sciences from Rice University in 2014, applying to the University of Texas at Austin the same year. He was accepted and started graduate studies in Geosciences at the Jackson School in August, 2014, completing his Doctorate the summer of 2019.

Permanent address: 3008 E 14th 1/2 St
Unit B
Austin, Texas 78702

This dissertation was typeset with LaTeX[†] by The Author.

[†]LaTeX is a document preparation system developed by Leslie Lamport as a special version of Donald Knuth's TeX Program.